Scaling of Single-Mode Operation in Lasers

Rushin Contractor

Electrical Engineering and Computer Sciences
University of California, Berkeley

December 15, 2023

Scaling of Single-Mode Operation in Lasers

By

Rushin Contractor

A dissertation submitted in partial satisfaction of the

requirements for the degree of

Doctor of Philosophy

in

Engineering – Electrical Engineering and Computer Sciences

in the

Graduate Division

of the

University of California, Berkeley

Committee in charge:

Professor Boubacar Kanté, Chair
Emeritus Professor Eli Yablonovitch
Professor Dan Stamper-Kurn

Fall 2023

Scaling of Single-Mode Operation in Lasers

Abstract

Scaling of Single-Mode Operation in Lasers

by

Rushin Contractor

Doctor of Philosophy in Engineering – Electrical Engineering and Computer Sciences

University of California, Berkeley

Professor Boubacar Kanté, Chair

Selecting a single optical mode in a cavity has been central to laser technology since its inception. Despite this, semiconductor lasers, crucial in a wide range of applications from consumer electronics to specialized medical and defense equipment, face significant challenges in maintaining single-mode operation, especially in larger cavities.

This thesis represents an interdisciplinary endeavor, merging semiconductor optics, photonic devices, electromagnetism, quantum mechanics, condensed matter physics, and atomic physics to engineer a laser that sustains single-mode operation regardless of cavity size. The core strategy involves a photonic crystal-based approach to enhance single-mode operation and the nature of wave confinement in cavities is also explored in the process. These advancements not only mark a significant step in laser technology but also open new potential for light-matter interaction in various scientific and technological domains.

"The sounds in my mind just come to me,
Come see..."

—Visions of Paradise, The Moody Blues

Contents

Acknowledgments

About 6 years ago, residing in a dingy Maryland rental, I faced an uncertain future with limited prospects. Getting a PhD and continuing to learn stood out as the most (if not the only) fulfilling option. So the first person I'd like to acknowledge in making this happen is my advisor Prof. Boubacar Kanté for bringing me here to the coasts and mountains of California, first to San Diego and then Berkeley. Just a few sunsets have indeed been worth the venture.

Over the course of this journey, I have been fortunate to interact, collaborate, and travel alongside amazing people from across the globe. Academic learning was bound to happen, but the cultural and social interactions have been even more valuable. Despite its many flaws, Berkeley certainly has played its part in enabling such experiences.

Among the more relevant skills I have developed, the ability to articulate and interpret scientific information more effectively stands out. For this I would like to thank everyone sitting in the most inhospitable corner of Cory—the 2nd floor mezzanine. It was really enlightening learning from and sharing knowledge over a wide range of topics with you all! My thanks also extend to Prof. Eli Yablonovitch, whose seasoned perspective lent a unique flavor to our group meetings.

Certainly, a few individuals in particular have had a more direct contribution to this thesis. There really wouldn't be a laser to write about without the countless hours Wanwoo, Emma, and Wayesh spent in the cleanroom operating complex machines and dipping tiny chips in toxic solutions. The nanolab staff at UCSD, Marvell, and Berkeley Lab especially Maribel and Scott have also been instrumental in their support. Furthermore, the work wouldn't come to fruition without Walid spending many a night in the optics labs characterizing and documenting the results from nearly every device.

Finally, I'd like to thank my immediate family and friends from the old world who have all been through various hardships over the last few unconventional years but still managed to stay together and support each other often over vast distances.

Chapter 1

Introduction

Semiconductor lasers have become integral component in modern society, underpinning a multitude of advancements that shape our daily lives and collective technological progress. In fact, most readers only have access to this thesis because of tiny lasers blinking rapidly and transmitting data across vast distances. They are used in a wide range of applications in industrial manufacturing, medical devices and surgeries, ranging and mapping, and defense. They also enable many of these functionalities to be integrated into consumer electronics such as phones (now equipped with exuisite capabilities for three-dimensional mapping) and watches (that monitor your health with lasers).

A critical feature for most of these applications is the ability to operate on a single cavity mode [1]. Conventional designs often struggle to maintain spectral purity, coherence, beam quality and power efficiency as the device is scaled up in size or power. This dissertation introduces a laser design based on photonic crystal cavities, adept at overcoming these limitations to achieve scalable single-mode operation irrespective of cavity size.

Central to this advancement is the unique geometry of the photonic crystal lattice, specifically tailored to exhibit a linear dispersion relationship known as a Dirac cone. This dispersion, coupled with open boundary conditions, forms what we term an 'open-Dirac potential'. The admixture of modes within this potential gives rise to distinctive cavity modes, the properties and characteristics of which are detailed in this thesis. These insights lay the groundwork for the design of the Berkeley surface-emitting lasers (BerkSELs) [2].

The dissertation is structured as follows. Chapter 1 lays the foundation, delving into the core idea in laser physics, electromagnetism, photonics, and wave behavior in periodic media. This sets the stage for understanding the intricacies of photonic crystal laser design. In Chapter 2, we explore key concepts in topological photonics: bound states in the continuum and Dirac cones, using these to develop the theoretical framework for the open-Dirac cavity. Chapter 3 presents the crux of the thesis, detailing the key results alongside the methodologies employed in simulation, fabrication, and characterization of BerkSELs designed so as to achieve robust single-mode operation. Concluding the narrative, Chapter 4 summarizes the developments discussed throughout the thesis, reflecting on the potential technological impacts of the BerkSEL and envisaging future avenues for research and application.

In our exploration, we will traverse various distinct yet interconnected domains in physics and engineering. It is thus critical to employ a consistent set of symbols and abbreviations to denote various physical quantities and mathematical concepts that are often presented very differently between these fields. The most common of course is the imaginary unit $\sqrt{-1}$ notated as i by physicists and j by engineers. Here, we use i since electric current is not a quantity we consider in much detail. Vectors are indicated by boldface notation, while matrices are represented in sans-serif font. Unit vectors and oprators are distinguished with a hat symbol, and operators, such as the Hamiltonian, are also denoted in calligraphic style.

Before we get into the bulk of the physics, we first need a basic understanding of the principles of operation of a laser.

1.1 Laser fundamentals

Lasers consist of two main components: a gain medium and a cavity [3]. The gain medium acts as a type of "fuel" amplifying light over a range of frequencies. The cavity selects one (or more) of these frequencies which then reach a threshold resulting in a light emission that is extremely monochromatic and coherent. The physical processes responsible for this phenomena are detailed in Fig. 1.1. The top row shows the bandstructure of a typical semiconductor. We will cover what this means in more detail in Section 1.2.3 but for now it will suffice to know that green electrons in the valence (lower) band are confined near the positively charged ions in the semiconductor crystal lattice. Hence, they move slowly and have less energy than purple electrons in the conduction (upper) band which are free to move around within the material.

When light is incident on a material, electrons in the valence band may absorb some of the photons that penetrate the material. This causes the electrons to gain energy equal to the energy of the absorbed photon. If the energy of the incident light is greater than the bandgap (energy difference between the valence and conduction bands) then electrons can be set free from the confines of their ions and end up in the conduction band. This is called pumping as the idea is similar to pumping water to from a lower elevation to a higher elevation. While the schematic (Fig. 1.1a) and discussion has focused on optical pumping, it is possible (and often desirable) to pump a semiconductor electrically by passing current.

Spontaneous emission can occur in such excited electrons due to quantum fluctuations and causes them to relax to a lower energy state while emitting a photon. We can think of many classical analogies to this process because even in classical mechanics, particles tend to stabilize in low energy state. For example, water flowing over a sieve will slowly seep through. Even in the case of electrons, it is not surprising that a positively charged ion may capture a freely moving electron. However, this process is inherently quantum mechanical in nature. The frequency (energy) and momentum (direction) of the photon emitted is determined probabilistically. If the gain medium is in a cavity, let's say a simple one consisting of two mirrors, then most of these spontaneously emitted photons will escape (Fig. 1.1b). However, some will have just the right properties, and remain confined by the cavity.
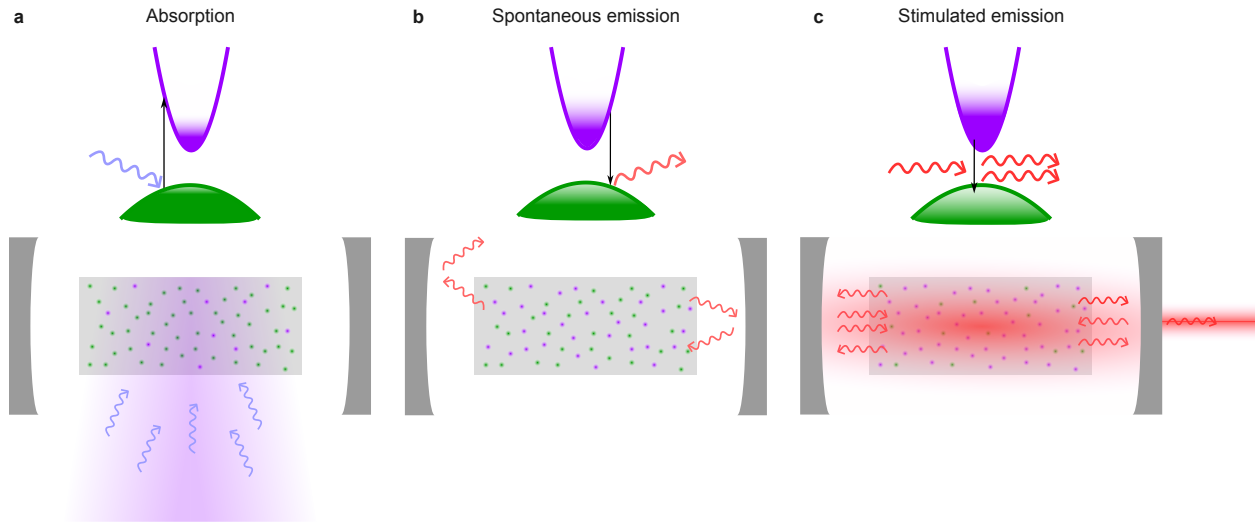
Figure 1.1: *Light-matter interaction in semiconductors and schematic of a laser cavity.* **(a)** Electrons in the valence band absorb photons and are excited to the conduction band. A material with particularly strong light absorption and emission tendency is placed in a cavity. Energy is supplied by an external laser to induce absorption or by applying a current to excite electrons to the conduction band. **(b)** Electrons in the conduction band can spontaneously emit photons along a random direction. This causes them to lose energy corresponding to the frequency of the emitted light and relax back to the valence band. Most of these photons escape, but some remain confined as determined by the properties of the cavity. **(c)** A photon passing through the gain medium may stimulate emission of an exact copy of the original photon and cause the electron to relax to the valence band. These photons can then induce further stimulated emission starting a chain reaction. If the cavity is partially transmissive, some of this light is coupled out and the device acts as a source of extremely directional monochromatic light.

Such photons bouncing around in the cavity can now induce emission of more photons with exactly the same frequency and momentum. This process is called stimulated emission. We could think of it as a vibrating spring inducing the same vibrations in another spring that is connected with it but again, the classical analogies are indeed a stretch and only serve to form an intuitive understanding. The real intricacies lie in the mathematical equations that describe these processes. Now we have a situation where some photons trapped in the cavity are causing the electrons to emit exact copies of themselves which then go around the cavity emitting even more copies resulting in a chain reaction. If some of this light in the cavity could be coupled out, we end up with a source of extremely directional and monochromatic light.

1.1.1 Rate equations

The theoretical foundations enabling the development of the laser were established in 1917 when Albert Einstein first described the quantum processes of absorption, spontaneous emission, and stimulated emission of electromagnetic radiation [4]. This work introduced Eintein's A and B coefficients that quantify atomic interactions with light. The rate of spontaneous emission is proportional to the number of electrons in the conduction band N_2 since more excited increases the probability that some of them will eventually relax. Photons with a frequency corresponding to an energy greater than the bandgap can either stimulate more atoms to relax while emitting more photons, or be absorbed by atoms already existing in the ground state. This rate of stimulated emission is thus proportional to the number of photons P and the difference in the number of electrons in the conduction and valence bands $N_2 - N_1$.

$$\frac{\mathrm{d}N_1}{\mathrm{d}t} = BP(N_2 - N_1)\,, \tag{1.1}$$

$$\frac{\mathrm{d}N_2}{\mathrm{d}t} = -AN_2 - BP(N_2 - N_1)\,. \tag{1.2}$$

These equations made physicists realize an intruiging possibility. If population inversion ($N_1 < N_2$) was achieved and the emitted photons were confined in a cavity, they would stimulate the emission of more and more identical photons. This would lead to an exponential growth in the intensity of light at a single frequency all directed at the same point in space. A device that achieves this is called a laser.

In most multi-level atoms and semiconductors, the pumping scheme (injection of atoms to the excited state) can be engineered to achieve $N_1 \ll N_2 = N$. The cavity rate equations can now be written as,

$$\frac{\mathrm{d}N}{\mathrm{d}t} = R - AN - N/\tau_n - BPN\,, \tag{1.3}$$

$$\frac{\mathrm{d}P}{\mathrm{d}t} = BPN + \beta AN - P/\tau_p\,. \tag{1.4}$$

Here, R is the pump strength, τ_n is the lifetime of the electrons in the excited state, β is the fraction of spontaneously emitted photons corresponding to the desired mode, and τ_p is the lifetime of photons in the cavity. We will not cover the possible solutions to these equations but depending on the various parameters, they could describe lasers, LEDs, photodetectors, and solar cells. Moreover, we must note that this is a gross oversimplification of the actual physics at play here. A first principles analysis would require knowledge of the full vectorial electromagnetic field as well as an understanding of the quantum states occupied by the electrons.

Having established the fundamental rate equations that underpin the operation of lasers, it becomes clear how these principles have been adapted and applied to create a diverse array of laser types, each tailored to specific applications and functionalities. Different types of

lasers may vary in their active medium, the method of pumping energy into that medium, and the specific engineering of the cavity. The first lasers were built using cavities with precisely arranged mirrors. Dyes, gases, and solid-state crystals were some of the first materials placed within the cavity to supply gain. For instance, gas lasers, such as the helium-neon, argon, or carbon-dioxide laser, rely on electrical discharges to excite atoms in a gas medium, while solid-state lasers use doped insulating materials to supply gain and are often pumped with light from other lasers or LEDs. Such schemes are still used today for specific applications. However, after the invention of semiconductor lasers in the 1970s they have become the standard for modern commercial laser devices.

Semiconductor lasers have become highly sought-after sources of coherent light, owing to their compact size, high efficiency, direct electrical pumping, and the capability to directly modulate the output beam. This is made possible by the arrangement of electrons within a semiconductor's lattice (Fig. 1.1). For mathematical simplicity, the motion of valence band electrons (green) is often represented by the movement of 'holes' they leave behind, which are effectively treated as positively charged particles. These gaps are called holes and for all practical purpose are treated as positively charged particles. Absorption, as depicted in Fig. 1.1a, causes some of the valence band electrons to gain some energy and they are set free from the ions. What makes semiconductor special in their interaction with light is that the energy needed to send one electron from the valence to the conduction band corresponds to the energy of photons in and around the visible spectrum of light. Moreover by controlling the properties of the lattice by adding impurities and strain, the frequency of the interaction can be tuned considerably.

Common configurations for semiconductor lasers include edge emitting lasers and vertical cavity surface emitting lasers (VCSELs). However, these traditional laser designs face challenges in scaling to high power without compromising beam quality and single-mode stability. Edge emitting lasers utilize cleaved semiconductor facets to form elongated cavities that support single transverse mode output but increasing the device length and aperture size leads to multiple longitudinal modes and beam quality degradation. VCSELs offer flexible scaling of the emission area but suffer from spatial hole burning effects as the aperture increases. This results in competition among multiple transverse modes impacting spatial coherence and mode stability. This inherent limitation in traditional cavity designs underscores the need for innovative approaches to achieve scalable single-mode operation. Motivating the need for novel solutions to overcome these challenges.

To fully grasp the innovative approach of photonic crystal lasers proposed in this dissertation, a thorough understanding of key electromagnetism principles and photonic lattices is essential.

1.2 Electromagnetism and photonics

Photonics encompasses the study of light and its interaction with matter, as well as its application in designing optoelectronic devices. While its name might imply a focus on the

quantum nature of light, in many areas of photonics, such as integrated photonics, a deep understanding of quantum theory is not always necessary. Devices like waveguides, splitters and couplers, ring resonators, and interferometers can be accurately designed using only a classical viewpoint of light as an electromagnetic wave. However, in applications involving quantum devices like photodetectors and single-photon sources, an understanding of the quantum nature of light becomes essential.

1.2.1 Schrödinger's equation

Our journey begins with Schrödinger's equation, a fundamental tenet of quantum mechanics. This equation describes how the quantum state of a physical system changes over time, encapsulating the wave-like nature of particles [5].

$$i\hbar\frac{\partial}{\partial t}|\psi(t)\rangle = \hat{\mathcal{H}}|\psi(t)\rangle\,, \tag{1.5}$$

where i is the imaginary unit, and $\hbar$ is the reduced Planck's constant. While this may seem any other wave equation, the interpretation of the wavefunction $|\psi(t)\rangle$ and the Hamiltonian $\hat{\mathcal{H}}$ are what set this equation apart. The quantum mechanical wavefunction is not a measurable or even a clearly definable quantity but encapsulates all the properties of a system. Typically, the wavefunction returns a measurable quantity by applying an operator on the wavefunction or projecting it on another known state. For example, $\langle x|\psi(t)\rangle = \psi(x,t)$ where $|x\rangle$ is an eigenstate localized at position x and $|\psi(x,t)|^2$ is the probability of finding a particle at position x and time t.

The Hamiltonian $\hat{\mathcal{H}}$ can now be understood as an operator that determines the time evolution of the wavefunction. The definition of $\hat{\mathcal{H}}$ for a system is related to the total energy of that system. While this may sound unintuitive at first, it can be simply be understood as the statement, "more energetic systems change more rapidly" and the time dependence of a wavefunction in a closed system is recorded as $|\psi(t)\rangle = |\psi_0\rangle e^{-i\mathcal{E}t/\hbar}$, where $\mathcal{E}$ is the energy of the system. With this in mind, we can take a closer look at a commonly used form of the time-independent Schrödinger's equation,

$$\mathcal{E}\psi(\boldsymbol{r}) = \left(\frac{\hat{\boldsymbol{p}}^2}{2m} + V(\boldsymbol{r})\right)\psi(\boldsymbol{r})\,. \tag{1.6}$$

Here, $\hat{\boldsymbol{p}} = -i\hbar\boldsymbol{\nabla}$ is the momentum operator, making $\hat{\boldsymbol{p}}^2/2m$ the kinetic energy of the system, and $V(\boldsymbol{r})$ is the potential at position $\boldsymbol{r}$.

Consider the case of a particle in a constant potential $V(\boldsymbol{r}) = 0$. Now it is possible to find a simple solution to Eq. (1.6):

$$\psi(\boldsymbol{r},t) = Ae^{i(\boldsymbol{k}\cdot\boldsymbol{r}-\omega t)}\,. \tag{1.7}$$

This function denotes a wave-like solution. The wavevector $\boldsymbol{k}$ represents the direction and rate of oscillations in space, and may be used interchangeably with the momentum, $\boldsymbol{p} = \hbar\boldsymbol{k}$.

The frequency of oscillations in time is proportional to the angular frequency ω which is often used interchaneably with the energy $\mathcal{E} = \hbar\omega$. The amplitude of the wave A is only meaningful relative other wavefunctions, or at boundaries between separate domains because if $A|\psi\rangle$ is a solution to a linear Hamiltonian, then so is $A'|\psi\rangle$. Such planewave solutions are not only crucial in quantum mechanics but also form a bridge to electrodynamics and mirror the wave nature of classical electromagnetic fields in a uniform region of space.

1.2.2 Maxwell's equations

Four equations put together by Maxwell in the year 1865 [6] encompass the core principles of electromagnetism, which govern nearly all of the physical interactions encountered in everyday life, barring gravitational forces.

$$\boldsymbol{\nabla} \cdot \boldsymbol{D} = \rho \,, \tag{1.8}$$

$$\boldsymbol{\nabla} \cdot \boldsymbol{B} = 0 \,, \tag{1.9}$$

$$\boldsymbol{\nabla} \times \boldsymbol{E} = -\frac{\partial \boldsymbol{B}}{\partial t} \,, \tag{1.10}$$

$$\boldsymbol{\nabla} \times \boldsymbol{H} = \boldsymbol{J} + \frac{\partial \boldsymbol{D}}{\partial t} \,. \tag{1.11}$$

Here, ρ is the electric charge density, $\boldsymbol{E}$ is the electric field, $\boldsymbol{H}$ is the magnetic field, $\boldsymbol{D} = \varepsilon\boldsymbol{E}$ is the displacement field, $\boldsymbol{B} = \boldsymbol{\mu}\boldsymbol{H}$ is the magnetic flux density, and $\boldsymbol{J}$ is the current density. The effect of the material in which these fields exist is taken into account via the permittivity $\boldsymbol{\varepsilon}$ and the permeability $\boldsymbol{\mu}$. The permittivity and permeability are tensors that depend on the local value of the fields themselves. However, in most cases they are approximated as real numbers. Dispersion, or the frequency dependence of the material properties, is often important and needs to be considered as well.

At a macroscopic level, the presence of net charges or currents is rare. So, we can assume $\rho = 0$ and $\boldsymbol{J} = 0$. In a region where the permittivity and permeability is isotropic, Eqs. (1.8) to (1.11) can be expressed as,

$$\nabla^2 \boldsymbol{E} = \mu\varepsilon \frac{\partial^2 \boldsymbol{E}}{\partial^2 t} \,, \tag{1.12}$$

$$\nabla^2 \boldsymbol{H} = \mu\varepsilon \frac{\partial^2 \boldsymbol{H}}{\partial^2 t} \,. \tag{1.13}$$

Moreover, if the material properties are only weakly affected by the fields (i.e. non-linear effects are not significant) we can investigate the solutions to Maxwell's equations independently by frequency. This means that $\boldsymbol{E}(\boldsymbol{r}, t) = \boldsymbol{E}(\boldsymbol{r})e^{i\omega t}$, where ω is the angular frequency, is a general solution and we obtain,

$$\left(\boldsymbol{\nabla}^2 + \omega^2\mu\varepsilon\right)\boldsymbol{E} = 0 \,. \tag{1.14}$$

This equation admits wave solutions similar to Eq. (1.7) where $k = |\boldsymbol{k}| = \omega/c$ is the wavenumber and $c = 1/\sqrt{\mu\varepsilon}$ is the phase velocity. In free space, this number $c_0 = 1/\sqrt{\mu_0\varepsilon_0} \sim 300$

µm THz is a fundamental constant of our universe. One way of looking at this is that if the electric (or magnetic field) are thought of as strings, then a 1 µm string would oscillate at a frequency of 300 THz. Note the units used here are the most convenient when working with light when the wavelengths of interest are from 0.4 µm to 2 µm.

The main difference between Eq. (1.6) and Eq. (1.14) is the fact that the later is a vector equation. So when we talk about electromagnetic waves, along with the direction of propagation, the orientation of the constintuent vector fields is also required to define a unique solution.[1] This property, known as the polarization, becomes especially critical when the material properties are anisotropic or change at the scale of the wavelength of light. Hence, for consistency across the thesis, we will only consider tranverse-electric (TE) polarization with the convention that the dominant field components are E_x, E_y, and H_z.

1.2.3 Waves in periodic media

Consider a region in space where the permittivity distribution obeys the function $\varepsilon(\boldsymbol{r} + \boldsymbol{a}) = \varepsilon(\boldsymbol{r})$. Equation (1.14) now supports a solution of the form,

$$\boldsymbol{E}(\boldsymbol{r}) = \boldsymbol{u}(\boldsymbol{r})e^{i\boldsymbol{k}\cdot\boldsymbol{r}} , \tag{1.15}$$

where $\boldsymbol{u}(\boldsymbol{r}) = \boldsymbol{u}(\boldsymbol{r} + \boldsymbol{a})$ is a function with the same period $\boldsymbol{a}$ as the permittivity distribution [7]. In fact, Eq. (1.15) also represents a plane wave, but one that is now modulated by the periodicity of the medium. We also note that the wavevector of the plane wave $e^{i\boldsymbol{k}\cdot\boldsymbol{r}}$ has an upper bound known as the Brillouin zone. This upper bound and its direction is not easy to imagine when the periodicity has a dimensionality larger than one so we will stick to one-dimensional periodicity when directly dealing with the mathematics, and then rely on computers to solve the equations in more complicated situations. For $\boldsymbol{a} = a\hat{y}$, oscillations of waves faster than $|k| = |\boldsymbol{k}\cdot\hat{y}| > \pi/a$ can simply be absorbed into the periodic function $\boldsymbol{u}(y)$ till the $k' = k - 2n\pi/a < \pi/a$, where n is an integer. A more detailed analysis of periodicity in two and three dimensions can be found in [8].

A binary grating with period a along the y-direction and fill factor f_1 is illustrated in Fig. 1.2. The permittivity is $\varepsilon(y) = \varepsilon_0$ for $|y| > f_1 a$ and $\varepsilon(y) = \varepsilon_1$ when $|y| \leq f_1 a$. However, the simplest periodic structure imaginable is a uniform region where $f_1 = 1$ or $\varepsilon_1 = \varepsilon_0$. If the permittivity is constant throughout space then we can assign any periodicity we want. An analytical solution for such a situation is not too difficult to find. Although to further simplify the math let us also set $E_y = 0$. Looking for a plane wave solution and substituting Eq. (1.15) in Eq. (1.14) for such a uniform region, we find that $\omega(k)/c = k + k'$ is a solution for $u(y) = e^{ik'y}$. We can now compute all possible ω for any given k within the Brillouin zone. The first four such frequencies are plotted using dotted lines in Fig. 1.2b. The real part of the Bloch function $u(y)$ at the high symmetry points $k_\Gamma = 0$ and $k_Y = \pi/a$ are also presented as insets in Fig. 1.2b. When studying an isolated electromagnetic field, the absolute phase of this field is not important and we can choose to consider either the real

---

[1] In the quantum mechanical picture, this appears in the form of a "spin" for the photon.

part or the imaginary part of the complex fields. Hence, at the high symmetry points the sine (odd) and cosine (even) Bloch functions have the same frequency. However, when two fields interact the relative phase between them does become significant and the imaginary component of the fields must be considered.
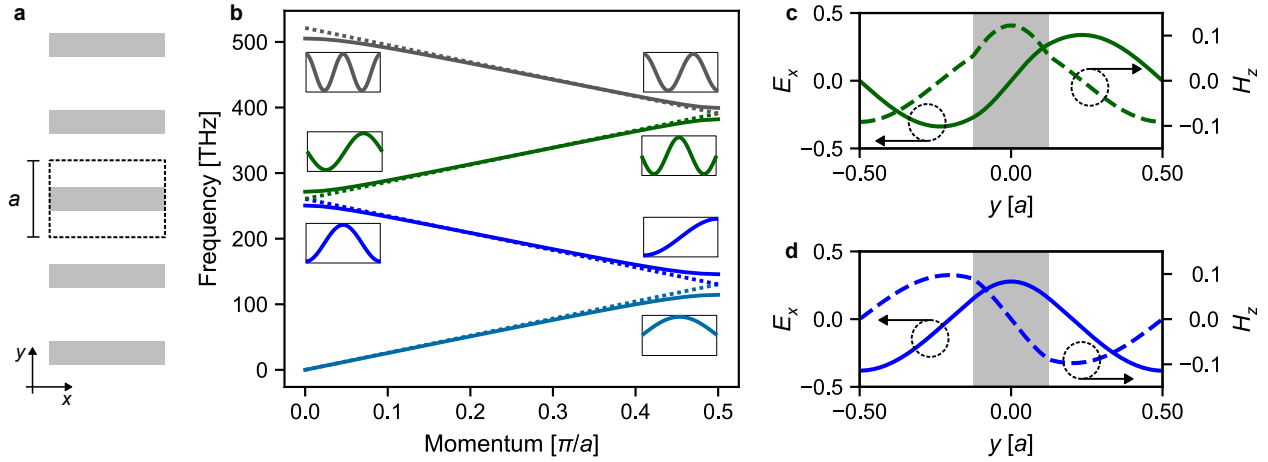

Figure 1.2: *Periodicity in one-dimension.* **(a)** Schematic representation of a one dimensional grating or photonic crystal with period a, fill factor f_1, and the relative permittivity of the two materials, ε_0 and ε_1. **(b)** Bandstructure of a grating with $a = 1\,\mu\text{m}$, $\varepsilon_1 = 2.25$, and $f_1 = 0.3$. The bandstructure of a uniform environment with average permittivity $\varepsilon = \varepsilon_0(1 - f_1) + \varepsilon_1 f_1$ is also presented with dotted lines. Insets show the distribution of the electric field at the high symmetry points $k_\Gamma = 0$ and $k_Y = 0.5\pi/a$. The solutions where the maxima of the electric field coincides with the region with larger permittivity take a lower frequency and the solutions where the maxima of the electric field coincides with the region with smaller permittivity index take a larger frequency than the two identical waves in the case of a uniform medium. **(c)** The electric and magnetic field distribution for the first odd mode at the Γ-point. **(d)** The electric and magnetic field distribution for the first even mode at the Γ-point.

Let us now introduce a perturbation to this uniform region. The solid lines in Fig. 1.2b represents the bandstructure for $f_1 = 0.25$ and $\varepsilon_1 = 2.25$. Now the sine and cosine solutions are no longer equivalent. The electric field for the cosine solution has its maxima at $y = 0$ which also coincides with the region with larger permittivity. Electric fields tend to be concentrated in regions high in permittivity (and magnetic fields tend to be concentrated in regions high in permeability) so the cosine has a lower energy (or frequency) than the sine solution. This opens up a band gap and frequencies within this gap cannot propagate in this medium. The electric (solid lines) and magnetic (dashed lines) field distribution for the lowest frequency even and odd Bloch wavefunctions at the Γ-point are presented in Fig. 1.2c,d. The zero frequency solution simply yields a constant (DC) field which does not

propagate as a wave so we will ignore that. Also, we choose to define the parity (odd-even nature) of the fields based on the electric field. The magnetic field has the opposite parity and from Section 2.3 onward, we will use the magnetic field for this purpose.

    With these theoretical foundations in place, the next chapter shifts our focus to exploring the distinct properties and behaviors of light in periodic media, unveiling new and unique optical phenomena.

Chapter 2

Patterns in light

A fundamental property of waves, including light, is their propagation through time and space. Yet, much effort has been devoted to confining these waves, as it opens up a plethora of applications in energy harvesting, sensing, detection, and coherent light emission. The simplest confinement method involves using reflective surfaces, such as mirrors, around a light source. In laser technology, this translates to aligning mirrors around the gain medium. However, maintaining precise mirror alignment is challenging, and even minor perturbations can significantly impact laser performance. Consequently, there has been a relentless pursuit of novel wave confinement methods.

This chapter explores one such technique, known as bound states in the continuum (BICs). The journey of BICs, from a quantum mechanical curiosity to a practical tool in photonics, illustrates how theoretical advances can lead to real-world applications. Readers primarily interested in the development of the BerkSEL may choose to skip the detailed exploration of BICs in Section 2.1. The subsequent discussion on Dirac cones, however, is integral to this thesis and does partially rely on Section 2.1.3. In Section 2.2, we delve into the conditions necessary to achieve Dirac cones and examine their properties. Building on this, Section 2.3 combines our understanding of BICs and Dirac cones to conceptualize the open-Dirac cavity.

2.1   Bound states in the continuum

Bound states play a pivotal role in the physics of fundamental particles, such as electrons in an atom or nucleons in a nucleus. Typically, these states occur when a particle's energy is lower than the surrounding potential, as detailed in classical physics and quantum mechanics [9]. For instance, an electron in a hydrogen atom will escape and ionize the atom if its energy surpasses the Coulombic attraction of the proton.

This conventional understanding, known in 1926 when Schrödinger introduced his equation, Eq. (1.5), was soon challenged by unexpected theoretical developments. In a ground-breaking work by von Neumann and Wigner [10], it was revealed that Schrödinger's equation

allows for classically forbidden bound states, where particles can remain confined even with energy levels exceeding the potential barriers. Initially deemed as merely mathematical curiosities due to their derivation from unphysical potentials, these bound states in the continuum, or BICs, gained substantial interest over the decades. It wasn't until Stillinger and Herrick's work that more realistic potential models admitting BICs were proposed, albeit still unachievable in practice [11]. The concept finally took a more applicable turn with Friedrich and Wintgen's research, which, based on Feshbach's resonance interference model, showed that BICs could arise in various systems [12].

As we proceed, we'll first take a moment to explore the genesis of bound and resonant scattering states within quantum mechanics, specifically through Schrödinger's equation, laying the groundwork for understanding the novel properties of BICs.

2.1.1 A quantum mechanics perspective

A one-dimensional potential well is one of the most simple systems to demonstrate many novel characteristics observable in the quantum regime. Usually, it is serves as an introduction to the quantization of energy levels to a student new to the quantum regime. A more advanced treatment in conjunction with scattering theory also provides an understanding of how a bound state differs from unbound states.

We consider a 1D potential function represented by,

$$V(y) = \begin{cases} -V_0, & |y| \leq D/2, \\ 0, & |y| > D/2. \end{cases} \tag{2.1}$$

The Schrödinger's equation for such a potential can be written separately for the two regions as,

$$-\frac{1}{2}\partial_y^2 \psi(y) - V_0 \psi(y) = \mathcal{E}\psi(y), \quad |y| \leq D/2, \tag{2.2}$$

$$-\frac{1}{2}\partial_y^2 \psi(y) = \mathcal{E}\psi(y), \quad |y| > D/2. \tag{2.3}$$

Here, ∂_y represents the spatial derivative along the y-coordinate and we are working in units of $\hbar^2/m = 1$. The solutions to these equations can be expressed in terms of forward- and backward-propagating plane-waves, and the wavefunction can be written as,

$$\psi(y) = \begin{cases} Ae^{ik_1 y} + Be^{-ik_1 y}, & y < -D/2, \\ Ce^{ik_2 y} + De^{-ik_2 y}, & |y| \leq D/2, \\ Fe^{ik_1 y} + Ge^{-ik_1 y}, & y > D/2. \end{cases} \tag{2.4}$$

Substituting Eq. (2.4) into Eq. (2.2), the wavenumbers k_1 and k_2 emerge as,

$$k_1 = \sqrt{2\mathcal{E}}, \qquad k_2 = \sqrt{2(V_0 + \mathcal{E})}. \tag{2.5}$$

First we focus only on the bound states of the potential $V(y)$ which means there are no incoming waves, and $A = G = 0$. The remaining constants B, C, D, and F can obtained by applying the continuity conditions on the wavefunction and its spatial derivative at $|y| = a/2$. After some algebra, this results in a transcendental equation,

$$\tan(k_2 a) = \frac{-2ik_1 k_2}{k_1^2 + k_2^2} \,, \tag{2.6}$$

which can be solved numerically. It is also apparent that the right hand side of the equation takes a real value only if and only if $-V_0 < E < 0$. Thus, bound states exist only at negative energies for this potential which is expected because from Eq. (2.1), states with $\mathcal{E} > 0$ lie in the continuum.

The probability density of finding a particle at position x is given by $|\psi(x)|^2$. Since the total probability to find the particle must sum to unity, the wavefunction is normalized as,

$$\int_{-\infty}^{\infty} |\psi(x)|^2 \, \mathrm{d}x = 1 \,. \tag{2.7}$$

We also note that from Eqs. (2.4) and (2.5) that if the energy is positive then this integral does not converge because the solutions in the semi-infinite region of space $|x| > a/2$ are non-decaying. In fact, the normalizability of the wavefunction is one of the necessary conditions for a bound state.

For a Hamiltonian consisting of the kinetic energy and a purely local potential, the solutions to the time-independent Schrödinger's equation fall in two categories: Below the continuum threshold, the eigenvalues are discrete and the eigenfunctions are square-integrable, while above that threshold the eigenvalues are continuous and the eigenfunctions are not normalizable [9]. This is a commonly accepted assumption. If the energy lies in the continuum the wavefunctions can be plotted using scattering theory. As these states are not bound and consist of outgoing waves, the coefficients of the incident waves must be non-zero to conserve the probability flux. The solution can be obtained by employing the scattering- or S-matrix approach to solve the system of linear equations arising from the continuity conditions at the boundary. The S-matrix can be computed for any finite potential distribution and is a function of the incident wavefunction energy which relates the scattered waves to the incoming waves as,

$$\begin{pmatrix} B \\ F \end{pmatrix} = \mathbf{S}(\mathcal{E}) \begin{pmatrix} A \\ G \end{pmatrix} \,. \tag{2.8}$$

In fact, the S-matrix also includes information about the bound states of the system. If we write Eq. (2.8) as,

$$\mathbf{S}^{-1}(\mathcal{E}) \begin{pmatrix} B \\ F \end{pmatrix} = \begin{pmatrix} A \\ G \end{pmatrix} \,, \tag{2.9}$$

then nontrivial solutions with B, $F \neq 0$ can exist in the absence of incident waves ($A = G = 0$) when $\det(\mathbf{S}^{-1}) = 0$ which are known as the poles of the S-matrix [13].

As an example, we choose $V_0 = 25$ and $D = 1$. Two discrete energies are obtained from the solution of Eq. (2.6) and a particle "trapped" in such a well can only exist in one of these states. The two blue curves in Fig. 2.1 are the normalized probability amplitudes $|\psi(y)|^2$ for these two bound states and the shaded area shows the potential distribution. The probability amplitudes have been plotted from the energies of their respective wavefunction along the y-axis. The orange curve represents the probability density of an unbound particle incident from the left ($E = 1.4V_0$, $A = 1$). The oscillating behavior for $y < -D/2$ is the result of interference between the incident and reflected wavefunctions. Oscillations appear in the well region due to reflection from the two boundaries. For $y > a/2$, the probability density is constant and equal to the transmission probability. Clearly, such a wavefunction cannot be normalized and it represents a state in the continuum.
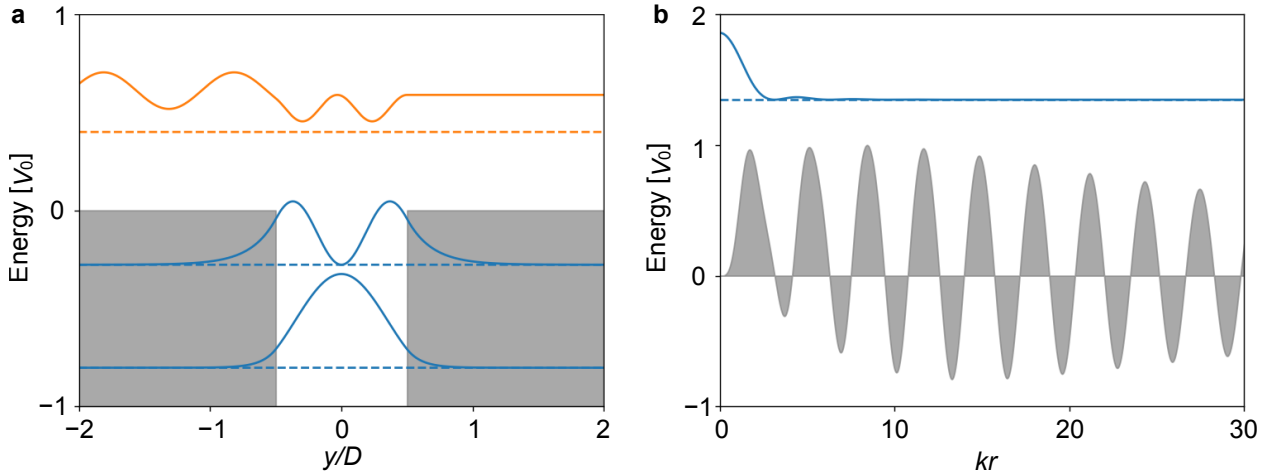

Figure 2.1: *Bound states, continuum states, and bound states in the continuum.* **(a)** Bound states and a wavefunction in the continuum for a 1D potential well. **(b)** Mathematically engineered potential that supports a bound state in the continuum. The wavefunctions are sketched from their respective energies on the y-axis. Note that the bound states have been normalized but the continuum state cannot be normalized and is scaled arbitrarily.

With this overview of bound states and the continuum in mind we can now examine the phenomena of bound states which exist within the continuum. Here, we first discuss von Neumann and Wigner's proposal which suggested the possibility of BICs as it was later improved and extended by Stillinger and Herrick. Let's make the potential $V(y)$ the subject in the Schrödinger's equation,

$$V(y) = \mathcal{E} - \frac{1}{2} \frac{\partial_y^2 \psi(y)}{\psi(y)} \ . \tag{2.10}$$

This means that for $V(y)$ to remain finite for all y, the Laplacian of the wavefunction $\partial_y^2 \psi(y)$ has to go to zero at the nodes of the wavefunction. An example of such a wavefunction is,

$$\psi_0(y) = \frac{\sin(ky)}{ky}, \tag{2.11}$$

which satisfies Eq. (2.10) with energy eigenvalue $\mathcal{E} = k^2/2$ for $V = 0$. Clearly, this wavefunction cannot be normalized and lies in the continuum of the potential V, but von Neumann and Wigner argue that if the amplitude of this wavefunction is modulated with another function that drops sufficiently rapidly with y, then this problem could be resolved. Thus, if

$$\psi(y) = \psi_0(y)f(y), \tag{2.12}$$

then ψ is square integrable if $f(y)$ drops to zero faster than y^{-p}, $\forall p > 1/2$. Substituting the modulated wavefunction into Eq. (2.10), we obtain

$$V(y) = \mathcal{E} - \frac{1}{2}k^2 + k\cot(ky)\frac{f'(y)}{f(y)} + \frac{1}{2}\frac{f''(y)}{f(y)}. \tag{2.13}$$

If the potential is to be finite and bounded, then the poles of $\cot(ky)$ must align with the zeros of $f'(y)/f(y)$. The specific choice first suggested was,

$$f(y) = \frac{1}{A^2 + [2ky - \sin(2ky)]^2}, \tag{2.14}$$

which can now be substituted in Eq. (2.10) to obtain the functional form of the potential. This potential depends on k will always support a bound state with positive energy $\mathcal{E} = k^2/2$. Unfortunately, this method cannot be used to compute any other wavefunctions or their energies analytically. However, as the potential vanishes at infinity, the scattering matrix method can be employed to calculate the wavefunction for unbounded particles. In Fig. 2.1, the potential from Eqs. (2.13) and (2.14) for $A = 25$ is shown by the shaded region and the corresponding wavefunction is also plotted from its energy along the y-axis. It is evident that a particle even with energy $\mathcal{E} > V_{\max}$ can be bounded in a finite region around the origin and the total probability amplitude its wavefunction can be normalized to unity.

The potential shown here has not been physically realized so far and it only serves as a simple proof of concept. It wasn't until the 1970s that interest in this phenomena was reignited when Stillinger and Herrick showed how such BICs can exist even in more meaningful potentials like engineered two-particle potentials or certain semiconductor lattices [14]. Finally, Friedrich and Wintgen showed the generality of this phenomena as an interference effect between two resonances [12]. They showed that if we have the freedom of varying the frequency separation between two resonances as a function of a continuous parameter then for certain value of the parameter, one of the resonances becomes a BIC. Using this intuition realistic models for BICs like a Hydrogen atom in a uniform magnetic field were also proposed by Friedrich [15].

Now with an understanding of bound states and a derivation for BICs in quantum mechanics, we are equipped to proceed towards Maxwell's equations.

2.1.2 Electromagnetism and bound states

Maxwell's equation do not admit BIC solutions in open systems extended over a finite region in space [16]. So most demonstrations are focused on extended structures which are periodic in atleast one direction. Various approaches were explored to achieve BICs in photonics [17–19] and an experimental demonstration based on photonic crystals soon followed [20]. In this section, we will use the coupled-wave analysis [21] and the scattering matrix approach [22] to understand the formation of not just BIC modes but also resonances and guided modes in periodic media like photonic crystals (PhC), just as we did for Schrödinger's equation.

The concept of a bound state needs to redefined for infinite periodic systems. Since the system extends to infity in one or more directions (the directions of periodicity) the normalization must be carried out over the remaining dimensions and a restricted domain like the unit cell for periodic strucutres. It is still possible to have quasi-BICs in finite systems like single particles or multiple coupled resonators by tuning the coupling between independent resonances. Such states are however not completely bound but are marked by a clear increase in the resonance lifetime [23]. We will briefly touch upon quasi-BICs in Section 2.1.3 but will first survey the mechanism of formation of bound states in the periodic media like photonic crystals using the coupled-wave theory [24].

Consider again the permittivity distribution from Fig. 1.2a but with a finite thickness h along the z-direction. The structure is confined in the region between $z = -h/2$ and $z = h/2$ but along the x-direction it is uniform and extends to infinity. The slab is also assumed to be embedded in an environment with uniform permittivity ε_0 and the system is symmetric in z.

The propagation of an electromagnetic wave with frequency $\omega = ck_0$ where c is the speed of light in the surrounding environment and k_0 is the magnitude of the momentum vector $\boldsymbol{k}$ in free space, can be expressed by the Helmholtz equation,

$$\boldsymbol{\nabla}^2 \boldsymbol{E}(y, z) + k_0^2 \varepsilon(y, z) \boldsymbol{E}(y, z) = 0 \,. \tag{2.15}$$

Here $\varepsilon(y, z)$ is the relative permittivity function. Since the permittivity is periodic ε obeys the relation,

$$\varepsilon(y + a, z) = \varepsilon(y, z) \,. \tag{2.16}$$

The permittivty can thus be expressed as a function of the reciprocal lattice period G with a Fourier transform as,

$$\varepsilon(y, z) = \sum_m \varepsilon'_m(z) e^{imGy} \,, \tag{2.17}$$

$$\varepsilon'_m(z) = \frac{1}{a} \int_0^a \varepsilon(y, z) e^{-imGy} \, \mathrm{d}y \,. \tag{2.18}$$

where G is defined as,

$$G = \frac{2\pi}{a} \, . \tag{2.19}$$

In the region with uniform permittivity only the zero-th order Fourier component is non-zero and $\varepsilon'_m(z) = \epsilon_0 \delta_m \, , \ \forall \ |z| > h/2$.

The Bloch function of the electric field at momentum $\boldsymbol{k} = k_x \hat{\boldsymbol{x}} + k_y \hat{\boldsymbol{y}}$ can also be expanded as a Fourier series,

$$\boldsymbol{u}_{\boldsymbol{k}}(y, z) = \sum_m \boldsymbol{u}'_m(\boldsymbol{k}, z) e^{i(k_y + mG)y} \, , \tag{2.20}$$

and the electric field can be expressed as,

$$\boldsymbol{E}_{\boldsymbol{k}}(y, z) = \sum_m \boldsymbol{u}'_m(\boldsymbol{k}, z) e^{ik_{ym}y} \, , \tag{2.21}$$

where,

$$k_{ym} = \boldsymbol{k} \cdot \hat{\boldsymbol{y}} + mG \, . \tag{2.22}$$

Introducing these transforms back into Eq. (2.15), we find a differential equation,

$$\partial_z^2 \boldsymbol{u}'_m(\boldsymbol{k}, z) = k_{ym}^2 \boldsymbol{u}'_m(\boldsymbol{k}, z) - k_0^2 \sum_n \varepsilon_{m-n}(z) \boldsymbol{u}'_{\boldsymbol{k},n}(\boldsymbol{k}, z) \, . \tag{2.23}$$

The electric field Bloch modes $\boldsymbol{u}'_m$ form an infinite basis, but the contributions from the higher order terms is negligible. Moreover, the z-direction evolution of each Fourier mode can be expressed as $\boldsymbol{u}'_m(\boldsymbol{k}, z) = \boldsymbol{u}'_m(\boldsymbol{k}) e^{i\beta_m z}$. This means that Eq. (2.23) can be expressed as an matrix equation after truncating the summation to a suitable number of Fourier orders,

$$-\boldsymbol{\beta}^2 \mathbf{u} = \hat{\boldsymbol{\mathcal{L}}} \mathbf{u} \, . \tag{2.24}$$

Here $\mathbf{u}$ is the a column matrix with the Fourier coefficients of the Bloch mode $\boldsymbol{u}'_m$, $\boldsymbol{\beta}^2$ is a diagonal matrix with the propagation constants β_m of the m-th Fourier coefficient, and $\hat{\boldsymbol{\mathcal{L}}}$ is a matrix form of the Maxwell operator obtained from the right handside of Eq. (2.23). Equation (2.24) is similar to the Schrödinger's equation and we can use the same approach used to solve for the wavefunctions of a potential well. However, if the permittivity is not a constant function, the operator $\hat{\boldsymbol{\mathcal{L}}}$ couples distinct Fourier components of the electric field through off-diagonal entries arising from the term ε_{m-n} in Eq. (2.23). Hence, we must first diagonlize this operator as,

$$\hat{\boldsymbol{\mathcal{L}}} = \mathbf{W} \boldsymbol{\beta}^2 \mathbf{W}^{-1} \, , \tag{2.25}$$

where $\mathbf{W}$ consists the eigenvectors of $\hat{\boldsymbol{\mathcal{L}}}$ as its columns, and $\boldsymbol{\beta}$ is a diagonal matrix with the square-root of the eigenvalues in the diagonal. For the region with uniform permittivity the

individual modes are uncoupled and $\mathbf{W} = \mathbf{I}$ is an identity matrix because $\varepsilon_{m-n} = 0$ unless $m = n$. Thus, the propagation constants α_m for the uniform regions are easily found to be,

$$\alpha_m = [\varepsilon_0 k_0^2 - k_x^2 - k_{ym}^2]^{1/2} \,. \tag{2.26}$$

This mathematical form of the incident and scattered waves on both sides of the periodic structure is shown in Fig. 2.2(b). The electric field can be expressed as a sum of forward- and backward-propagating waves in the periodic region. Since we are interested in resonant states of the PhC, we assume no incidence or $\mathbf{i}^+ = \mathbf{i}^- = 0$. Also, due to the symmetry in z, the boundary conditions need to be satisfied at only one interface and $\mathbf{c}^+ = \pm\mathbf{c}^- = \mathbf{c}$ are the amplitudes of the Fourier modes within the periodic region. The continuity of the tangential electric field and its derivative at $z = h/2$ results in the following equations.

$$\mathbf{W}(\mathbf{X} \pm \mathbf{X}^{-1})\mathbf{c} = \mathbf{t} \,, \tag{2.27}$$

$$\mathbf{W}\boldsymbol{\beta}(\mathbf{X} \mp \mathbf{X}^{-1})\mathbf{c} = -i\boldsymbol{\alpha}\mathbf{t} \,. \tag{2.28}$$

Here, $\mathbf{X} = \exp(-i\boldsymbol{\beta}h/2)$, and $\mathbf{t}$ contains the amplitude coefficients for each Fourier component in the transmitted wave. An intuitive way to think of these equations is that $\mathbf{W}$ projects the modes of the periodic region to plane wave basis, $\mathbf{X}$ propagates them to the boundaries, and $|C\rangle$ contains the relative amplitude of each mode to give the total electric field at the boundary. Eliminating $\mathbf{t}$ from these equations we obtain,

$$\left[\mathbf{W}\boldsymbol{\beta}(\mathbf{X} \mp \mathbf{X}^{-1}) + i\boldsymbol{\alpha}\mathbf{W}(\mathbf{X} \pm \mathbf{X}^{-1})\right] \mathbf{c} = 0 \,. \tag{2.29}$$

This equation can have non-trivial solutions if the determinant of the matrix that multiplies with $\mathbf{c}$ goes to 0. Thus, we obtain an equation similar to the transcendental equation Eq. (2.6),

$$f(\boldsymbol{k}) = \det\left[\mathbf{W}\boldsymbol{\beta}(\mathbf{X} \mp \mathbf{X}^{-1}) + i\boldsymbol{\alpha}\mathbf{W}(\mathbf{X} \pm \mathbf{X}^{-1})\right] = 0 \,. \tag{2.30}$$

Due to the assumption of symmetry, the same equation is valid for the boundary at $z = 0$, but if the symmetry is broken then we need to consider all four equations arising from the two boundaries to define $f(\boldsymbol{k})$. The solution to these equation yields the band diagram or $\omega(k)$ dispersion relation of the system. The frequency information can be obtained from the magnitude of the wavevector and the in-plane component from its direction.

If $\boldsymbol{\alpha}$ contains only imaginary entries then the corresponding resonance does not interact with the continuum and is a bound state. Hence, $f(\boldsymbol{k})$ can be a complex function and the solutions are scattering states where the frequency of the resonance $\omega = \omega_{\mathrm{r}} - i\gamma/2$ lies in the lower half of the complex plane. The imaginary part of this frequency signifies the decay rate. A bound state, which is non-decaying mode may hence be viewed as resonances with infinite lifetime and the decay rate γ must vanish for a bound state. In general $\boldsymbol{\alpha}$ may contain real entries if $k_y < \epsilon_0 k_0$. However, if α_m is real and $T_m \neq 0$ for some m, then there
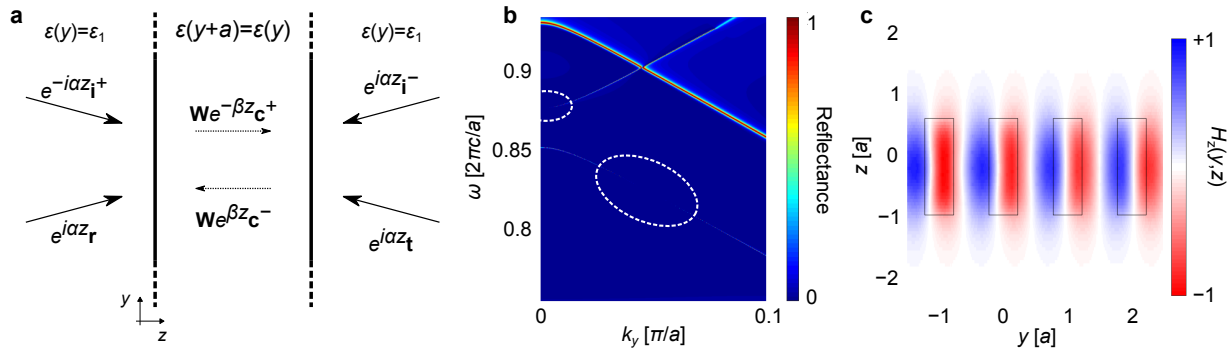
Figure 2.2: *Coupled wave analysis and simulation of BICs in a one-dimensional grating.* **(a)** Schematic represntation of the relevant mathetical terms involved in coupled-wave analysis of a periodic grating. **b** Reflectance spectrum of a grating with period $a = 1$ µm, permittivity $\varepsilon_1 = 2.1$, and thickness $h = 1.5$ µm. **(c)** Magnetic field distribution for the BIC mode at $k_y = 0.05\pi/a$.

exists a Fourier component of the fields that is allowed to propagate and this will induce a leakage channel that couples the resonance to the continuum. Thus, if there exists some real-valued α_m in $\boldsymbol{\alpha}$, then γ goes to 0 only if $T_m = 0$. This means that the resonance is a BIC.

If the system is not symmetric, or cannot be modelled with a single layer, the analysis can be carried out using the S-matrix. After some algebra, it is possible to write the scattered waves in terms of the incident waves as,

$$\begin{pmatrix} \mathbf{r} \\ \mathbf{t} \end{pmatrix} = \mathbf{S} \begin{pmatrix} \mathbf{i}^+ \\ \mathbf{i}^- \end{pmatrix} . \tag{2.31}$$

Now if **S** can be formulated, the problem is once again reduced to finding the poles of the S-matrix [25]. As with the function $f(\boldsymbol{k})$, the poles of S-matrix also have a negative imaginary part but for bound states the poles turn purely real and if α_m is real, the bound state is a BIC.

For the case of non-zero incidence, the S-matrix also serves as an efficient tool to compute the reflectance and transmittance efficiencies. The linewidth of a resonance in the reflectance or transmittance spectrum is dictated by the imaginary part of the resonant frequency γ. Since $\gamma \to 0$ around a BIC mode, the resonance passes through a region with zero linewidth. This can be seen clearly in the reflectance spectrum shown in Fig. 2.2b. Here, we demonstrate the existence of BICs in a structure with dielectric regions of permittivity 2.1 and thickness 1.5 µm arranged in a periodic array with a period of 1 µm and fill factor $f_1 = 0.4$. Moreover, from the solution of Eq. (2.30) we can also obtain the modes propagating within the structure from **c**. This allows us to visualize the field profile of the BIC mode shown in Fig. 2.2c for the resonance with zero linewidth at $k_y = 0.05\pi/a$.

2.1.3 Topology and symmetry

The coupled-wave analysis we just carried out gives a rigourous look at the origin of BICs. However, it can be difficult to visualize this destructive interference between the many Fourier components of these eigenmodes. A simpler picture can be found under some special circumstances. Let us take a closer look at the field distribution of the two modes plotted in Fig. 1.2. The polarization of the far field along the z-direction is determined by E_x. For the odd mode presented in Fig. 1.2c, the electric field at $-y$ perfectly cancels out the electric field at y. Thus, this mode cannot be accessed from the continuum via reflectance or transmittance measurements and does not radiate into the far field. Such a state is often called a dark mode or a symmetry-protected BIC. Note that for the even mode, the presence of the dielectric in the grating breaks the symmetry between the regions of the unit cell with positive and negative electric fields. This mode can indeed radiate to the far field and appears as an artifact in the reflectance/transmittance spectrum.

Consider the two-dimensional unit cell shown in Fig. 2.3a and adapted from [26]. When the width of two silicon bars is equal, $w_1 = w_2$, then a mode with odd symmetry along the y-direction will not radiate. As the width of one of the bars is changed however, then the symmetry of the structure and the electric field is broken and a resonce starts to appear in the reflectance spectrum as shown in Fig. 2.3b. When the difference in the width of the bars is small, the loss rate of the odd mode will be low and a sharp artifact appears in the spectrum. Such a mode is often called a quasi-BIC. The magnitude of the magnetic and electric field for a design with $w_1 \neq w_2$ is mapped in Fig. 2.3d,e to demonstrate the asymmetric nature of the fields. This design was used as a sensor to detect the presence of exosomes in an analyte by calibarating the shift in the frequency of the quasi-BIC resonance to a change in the refractive index [26].

These principles of symmetry are inherent to BICs and they represent states that are nontrivially topological in nature. This property is difficult to observe in the scalar wavefunctions of quantum mechanics, but when a BIC arises in a vector field it becomes apparent that these modes are associated with a nontrivial topological charge. The vector electric field is expressed in terms of the Fourier coefficients $\boldsymbol{u}'_m$ of Bloch waves $\boldsymbol{u_k}$ according to Eq. (2.21). For resonances that lie in the continuum but below the diffraction limit, only the zeroth order Fourier component can radiate, i.e. α_m is real only if $m = 0$. Hence, the propagating field can be obtained from the zero-th order Fourier coefficient of the transmitted wave, $\boldsymbol{t}_0$. Following the development in Ref. [27], we denote the in-plane polarization of the radiating electric field as,

$$\boldsymbol{E}_{\text{far}}(\boldsymbol{k}) = \boldsymbol{t}_0(\boldsymbol{k}) \cdot \hat{\boldsymbol{x}} + \boldsymbol{t}_0(\boldsymbol{k}) \cdot \hat{\boldsymbol{y}} \,. \tag{2.32}$$

However, we conluded from the coupled-wave analysis that for a mode to be a BIC $\boldsymbol{t}_0$ must equal zero if α_0 is real. Thus we must obtain a zero crossing of both, the x-component and the y-component of the polarization at the BIC point in k-space. Of course, this holds true even if more than one Fourier component can radiate and there exists at least one direction in $\boldsymbol{k}$-space along which tranversing from the BIC will maintain $\boldsymbol{E}_{\text{far},x} = 0$ and another direction
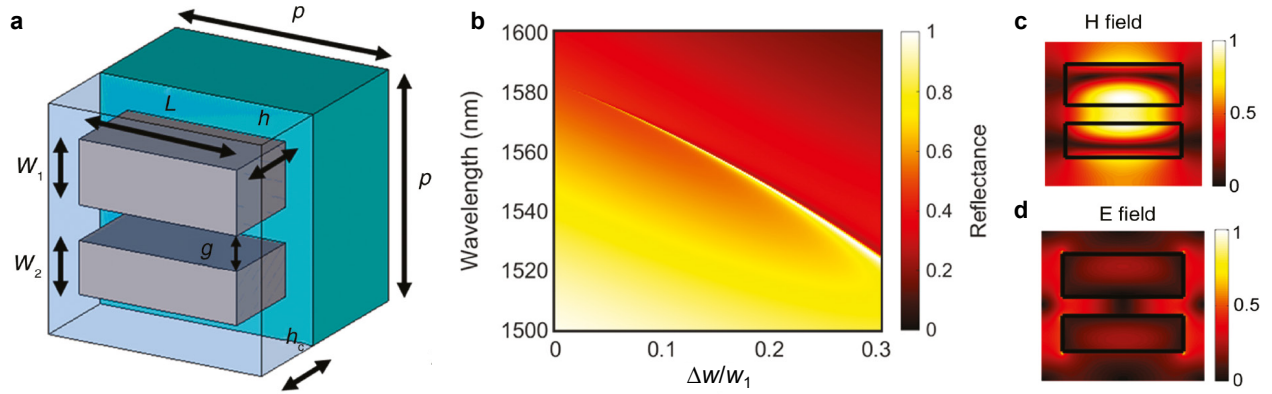
Figure 2.3: *Sensor based on symmetry-protected bound states in the continuum.* **(a)** Geometry of unit cell. The width of the Silicon bars, w_1 and w_2 are changed to tune the quality factor of the sensor. The frequency shift of the resonance is measured to quantify the biological analyte. **(b)** The resonance vanishes from the reflectance spectrum when $w_1 - w_2 = \Delta w = 0$ denoting the presence of a bound state in the continuum (BIC). When $\Delta w \neq 0$, a quasi-BIC resonance appears in the spectrum. **(c,d)** The magnetic and electric field distribution for a unit cell with asymmetric bars.

for which $\boldsymbol{E}_{\mathrm{far},y} = 0$. In fact the situation can be understood as an intersection of the nodal lines for $\boldsymbol{E}_{\mathrm{far},x} = 0$ and $\boldsymbol{E}_{\mathrm{far},y} = 0$ and extending the analogy to all possible directions we arrive at the conclusion that the polarization angle rotates around the BIC point.

Earlier in this section, we argues that the lowest order odd mode for a one-dimensional lattice (Fig. 1.2c) is a symmetry-protect BIC. We can visualize this winding of the electric field vector in the far field for this mode from Fig. 2.4. The polarization vector can be defined as,

$$\phi(\boldsymbol{k}) = \boldsymbol{E}_{\mathrm{far},x}(\boldsymbol{k}) + i\boldsymbol{E}_{\mathrm{far},y}(\boldsymbol{k}) , \qquad (2.33)$$

and $\arg[\phi]$ yields the polarization angle which is plotted in Fig. 2.4a. The arrows indicate the vector $\phi(\boldsymbol{k})$ which is actually the projection of $\boldsymbol{E}_{\mathrm{far}}$ on a circular polarization basis. This is demonstrated in Fig. 2.4b where the entire polarization ellipses are drawn with the color indicated the phase of ωt in full time cycle of the electric field. The vortex nature of BICs can now be quantized with a winding number defined as,

$$q = \frac{1}{2\pi} \oint \mathrm{d}\boldsymbol{k} \cdot \nabla_{\boldsymbol{k}} \arg[\phi(\boldsymbol{k})] . \qquad (2.34)$$

To compute this quantity we take a closed path in k-space that encircles the BIC under investigation and integrate the polarization angle along that contour. If more than one vortex is enclosed the winding number will be the sum of the inding number of every vortex within this region.
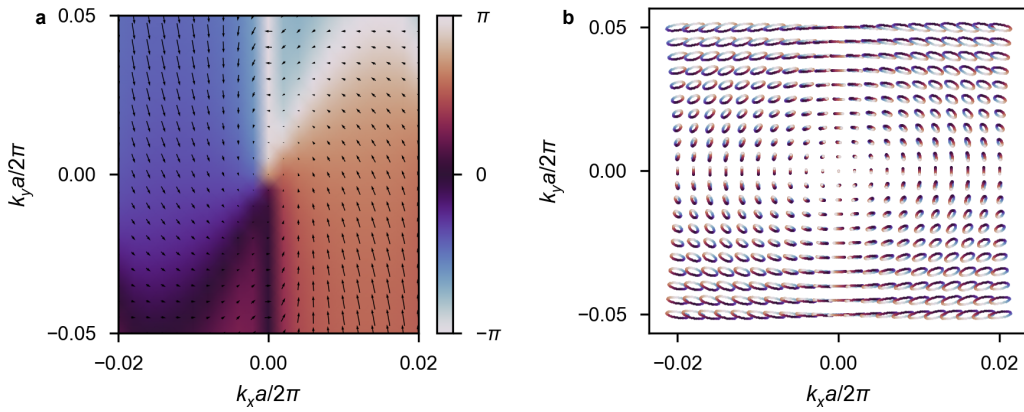
Figure 2.4: *Visualizing the polarization vortex around BICs.* **(a)** The polarization angle and projection of the electric field vector in the far field on a circular polarization basis. **(b)** The entire polarization ellipse obtained when the electric field completes one full time cycle. The colors indicate the phase within this cycle.

Similar analysis has also been done using electromagnetic multipoles as the bases of the radiating fields [28] and the zeros of the multipole radition pattern in polar coordinates show similar topology as the vortex nature found from the analysis in Fourier bases [29]. Another interesting conlusion from this observation is that these charges are always conserved during continuous changes in the geometric or material parameters that maintain the topology of the system. Hence, if a certain set of parameters supports a BIC, it cannot be destroyed by a continuous change in these parameters but the BIC may shift in frequency or momemtum.

Having explored the intriguing topological properties of bound states in the continuum, we now turn our attention to another significant topological phenomenon that has garnered widespread interest across multiple fields, including photonics, acoustics, and condensed matter physics: the Dirac cone. Initially discovered in the context of electrons in graphene, Dirac cones represent a key area of research due to their unique properties and implications for wave systems.

2.2 Dirac Cones

Dirac points are topological singularities that have captivated researchers since the identification of massless Dirac fermions in graphene, which revolutionized our understanding of electronic transport [30]. They are often indicative of a looming topological transition and play a crucial role in the physics of topological insulators [31]. Wave systems with a band structure, such as photonic crystals, commonly exhibit Dirac cones and it has been demonstrated that they are universal features that can be systematically implemented by

controlling the symmetry of the structure [32, 33]. In photonics, the exploration of Dirac cones has predominantly focused on realizing effective zero-index materials, manipulating their dispersion properties, and influencing polariton behavior [34–39]. Our next step is to delve into the formation of Dirac cones based on symmetry principles, subsequently applying these insights to engineer a Dirac dispersion in a one-dimensional lattice.

2.2.1 Perturbation theory

Let us apply the Bloch theorem to Schrödinger's equation. If we express the functional form of k-dependent Bloch wavefunctions $|\pm\rangle_k$ as $u_{\pm,k}(y)$, then for a particle moving in a periodic potential $V(y) = V(y + a)$,

$$\hat{\mathcal{H}}_0 u_{\pm,k}(y) e^{iky} = \left[-\frac{\hbar^2}{2m}\partial_y^2 + V(y) \right] u_{\pm,k}(y) e^{iky} \,. \tag{2.35}$$

Note that the modes possess a clear even $|+\rangle$ or odd $|-\rangle$ symmetry only at the Γ-point. As the wavefunctions are perturbed by the presence of a Bloch momentum, this symmetry may be broken. The Bloch functions themselves are eigenstates of the operator,

$$\left[-\frac{\hbar^2}{2m}\partial_y^2 + V(y) - \frac{i\hbar k}{m}\partial_y + \frac{\hbar^2 k^2}{2m} \right] u_{\pm,k}(y) = \left[\hat{\mathcal{H}}_0 + \hat{\mathcal{H}}_k \right] u_{\pm,k}(y) = \mathcal{E}_\pm(k) u_{\pm,k}(y) \,. \tag{2.36}$$

If k is small then we can ignore higher-order effects and $\hat{\mathcal{H}}_k = -(i\hbar^2 k/m)\partial_y$ is the first-order perturbation strength. The Bloch states $|\pm\rangle_k$ then satisfy,

$$\hat{\mathcal{H}}|\pm\rangle_k = \left[\hat{\mathcal{H}}_0 + \hat{\mathcal{H}}_k \right] |\pm\rangle_k = \mathcal{E}_\pm(k)|\pm\rangle_k \,, \tag{2.37}$$

where the unperturbed even $|+\rangle$ and odd $|-\rangle$ states satisfy $\hat{\mathcal{H}}_0|\pm\rangle = \mathcal{E}_\pm|\pm\rangle$.

The Hamiltonian $\hat{\mathcal{H}}$ can be expressed in the $|\pm\rangle$ basis as follows,

$$\hat{\mathcal{C}} = \sum |\pm'\rangle\langle\pm'|\hat{\mathcal{H}}|\pm\rangle\langle\pm| = \sum \langle\pm'|\hat{\mathcal{H}}|\pm\rangle|\pm'\rangle\langle\pm| \,,$$

$$\implies \hat{\mathcal{C}} = \begin{pmatrix} \langle+|\hat{\mathcal{H}}|+\rangle & \langle+|\hat{\mathcal{H}}|-\rangle \\ \langle-|\hat{\mathcal{H}}|+\rangle & \langle-|\hat{\mathcal{H}}|-\rangle \end{pmatrix} \,. \tag{2.38}$$

The derivative operator in $\hat{\mathcal{H}}_k$ changes the symmetry of the state. Thus, the off-diagonal matrix elements are non-zero if $|+\rangle$ and $|-\rangle$ have opposite symmetries, and we also have,

$$\langle\mp|\,\hat{\mathcal{H}}_0\,|\pm\rangle = \langle\pm|\,\hat{\mathcal{H}}_k\,|\pm\rangle = 0 \,. \tag{2.39}$$

While the exact form of $\hat{\mathcal{H}}_k$ is different for the Maxwell operator, the same arguments based on symmetry are still valid [32, 33].

To simplify the math, we now express $\hat{\mathcal{C}}$ as,

$$\hat{\mathcal{C}} = \begin{pmatrix} -\delta & -iMk \\ iM^*k & \delta \end{pmatrix}, \tag{2.40}$$

where $\delta = (\mathcal{E}_- - \mathcal{E}_+)/2$ and $M = i\langle -|\hat{\mathcal{H}}_k|+\rangle$ is the coupling strength. The eigenvalues of $\hat{\mathcal{C}}$ reveal the dispersion of the system and the eigenvectors are the orthogonal basis for the perturbed system projected onto the unperturbed state vector $\left(|+\rangle \quad |-\rangle\right)^{\mathrm{T}}$. When $\Delta = \delta/M \gg k$ the bands edges are quadratic. This is shown in Fig. 2.5a where the blue line indicates the frequency of the even mode and the green line indicates the frequency of the odd mode. As $\Delta \to 0$ the eigenvalues of $\hat{\mathcal{C}}$ become linearly dependent on k and a Dirac cone can be achieved as observed in Fig. 2.5b.
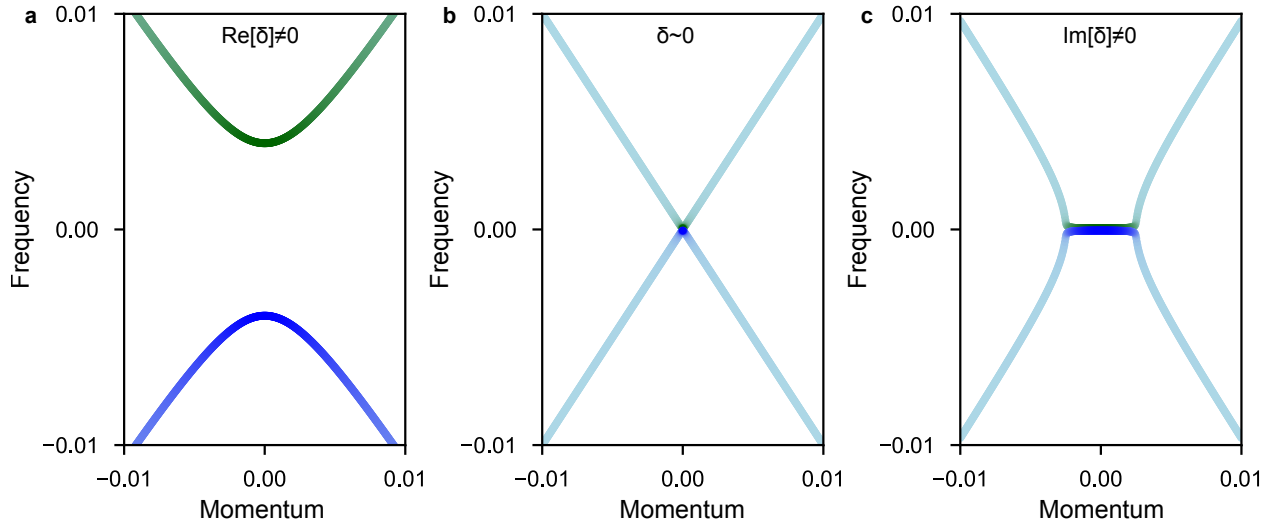

Figure 2.5: *Effect of detuning in the real- and imaginary-part of the frequency near the Dirac point.* **(a)** Quadratic band edges appear due to detuning in the real-part of the resonance frequencies of the even and odd modes. **(b)** A Dirac cone is obtained when the detuning $\delta \to 0$. **(c)** Detuning in the imaginary part of the frequencies results in a square-root dispersion with two exceptional points where the bands meet.

Moreover, the orthogonal solutions for the Bloch wavefunctions obtained as the eigenvectors of $\boldsymbol{C}$ are no longer the purely odd or purely even but an admixture of the two as shown in Fig. 2.8c by the light blue lines. We can express the new wavefunctions of the upper and lower bands as,

$$\mu_{\Delta,k}(y) = ic_{\Delta,k}u_+(y) + u_-(y), \tag{2.41}$$

$$\nu_{\Delta,k}(y) = u_+(y) + ic_{\Delta,k}u_-(y). \tag{2.42}$$

Here,

$$c_{\Delta,k} = \frac{\Delta}{k} - \sqrt{1 + \left(\frac{\Delta}{k}\right)^2}, \tag{2.43}$$

and from symmetry of $\hat{\mathcal{C}}$, we can say that $c_{\Delta,-k} = -c_{\Delta,k}$.

2.2.2 A Dirac grating

To visualize this, let us return the one dimensional grating from Fig. 1.2. Based on our analysis, we can predict that if the odd and even modes Fig. 1.2c,d are tuned to a degeneracy, the dispersion near the band edge at $k = 0$ will become linear. To achieve we introduce another grating shifted by half a period from the initial design as shown in Fig. 2.6a. In Fig. 1.2 we noticed that the even mode has a lower frequency than the odd mode because the maxima of the electric field coincides with the dielectric region. Now if we add another dielectric when $0.5 - |y| < f_2 a$ then the frequency of the odd mode should decrease more than the frequency of the even mode. We find that for $f_2 \sim 0.6$ and $\varepsilon_2 = 6.25$, degeneracy is achieved and the dispersion turns linear as expected.
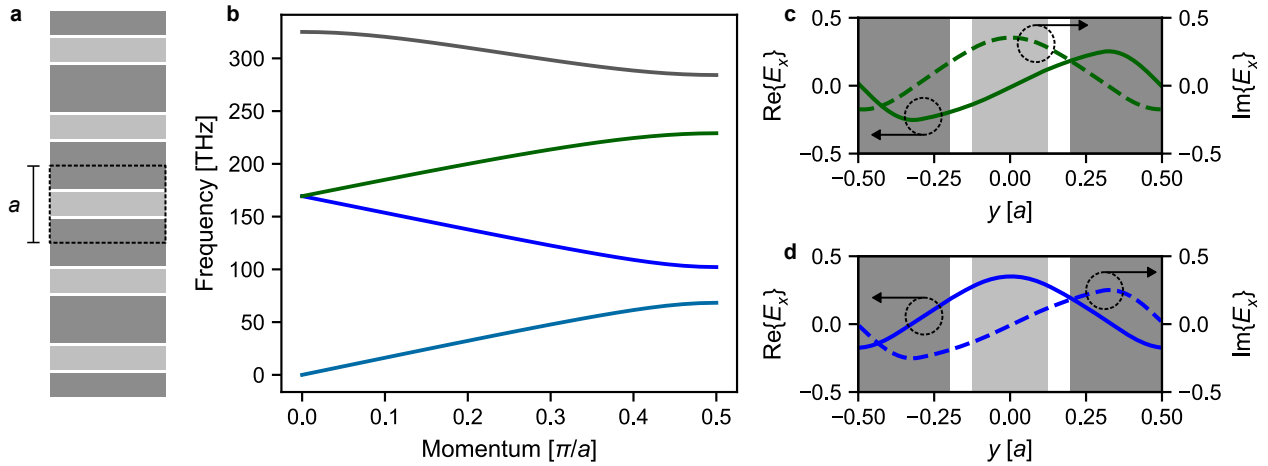

Figure 2.6: *Dirac cone in a one-dimensional lattice.* **(a)** Schematic representation of a one dimensional grating or photonic crystal with period a and three different materials. **(b)** Bandstructure of a grating with $a = 1\,\mu m$, $\varepsilon_1 = 2.25$, $\varepsilon_2 = 6.25$, $f_1 = 0.3$, and $f_2 = 0.6$. A Dirac point is created around the frequency of $170\,THz$. **(c)** The real (solid lines) and imaginary (dashed lines) component of the electric field for the upper band at $k_y = 0.01\pi/a$. **(d)** The real (solid lines) and imaginary (dashed lines) component of the electric field for the lower band at $k_y = 0.01\pi/a$.

The mixing of the photonic modes can also be verified from the field distributions. Upon introducing a small non-zero Bloch momentum, we expect that the electric field distribution

from the odd mode would appear in the imaginary component of the even mode and vice-versa because $c(0, k) = -1$. This can be observed in Fig. 2.6c,d where the real and imaginary parts of the electric fields for the two modes at $k = 0.01\pi/a$ are plotted. Note that $c(0, 0)$ is not uniquely defined because in the degenerate subspace, any linear combination of $|+\rangle$ and $|-\rangle$ is a valid solution. Here, we choose to set $c(0, 0) = 0$ because this is consistent with the non-degenerate case, $c(\Delta, 0) = 0$ when $\Delta \neq 0$.

However, we need to keep in mind that so far we only managed to tune the real part of the frequencies to a degeneracy. This is sufficient for the grating in Fig. 2.6, because the system is closed and there are no material or radiative losses being considered. A more practical design would be a grating with a finite thickness along the z-direction such as the one considered in Fig. 2.2b,c. During the discussion on symmetry-protected BICs we realized that the even mode can radiate. Hence, if the system is opened up to radiative losses along the z-direction then the imaginary part of the frequency of the odd and even modes would no longer be equal. This situation is covered in Fig. 2.5c. Here we find that in the presence of imaginary δ, the Dirac cone is distorted into a square root dispersion. The points at which the two bands meet are called exceptional points and have been demonstrated to be particularly effective sensors. For a laser however, stability is critical and a highly sensitive exceptional point is not ideal.

The two-dimensional periodicity in photonic crystals however, can guarantee a degeneracy in the loss rates as well. A comprehensive survey of all possible symmetries in various lattices has been carried out by mathematicians and find extensive use in understanding the properites of molecules, polymers, and solids [40, 41]. Here, we focus on the hexagonal or C_{6v} lattice and its character table is reproduced in Table 2.1. This table lists all the possible symmetry operations that keep the do not change the lattice in the header row. For example, the C_3 operation corresponds to rotation by $120°$, while the σ_x and σ_y operations are mirrors along the x- and y-directions respectively. The $+2$ for the identity operation E indicates a double degeneracy. Based on these symmetries it is possible to predict which of these modes radiate by computing the overlap integral with a plane wave propagating in the desired direction. At the Γ-point, only the E_1 modes radiate and all other modes are symmetry-protected BICs with a purely real resonant frequency.

Table 2.1: *Character table for the C_{6v} point group.*

Symmetry	E	C_6	C_3	C_2	σ_x	σ_y
A_1	+1	+1	+1	+1	+1	+1
A_2	+1	+1	+1	+1	-1	-1
B_1	+1	-1	+1	-1	+1	-1
B_2	+1	-1	+1	-1	-1	+1
E_1	+2	+1	-1	-2	0	0
E_2	+2	-1	-1	+2	0	0

The tranverse-electric (TE) modes in a hexagonal PhC around the $\Gamma^{(2)}$-point are pre-

sented in Fig. 2.7. The effect of the symmetry operations from Table 2.1 can be better understood by visualizing the rotation or mirroring of the fields from Fig. 2.7a. If the red region coincides with the blue region after a particular operation then that operation for the corresponding mode gets a -1 in the character table.
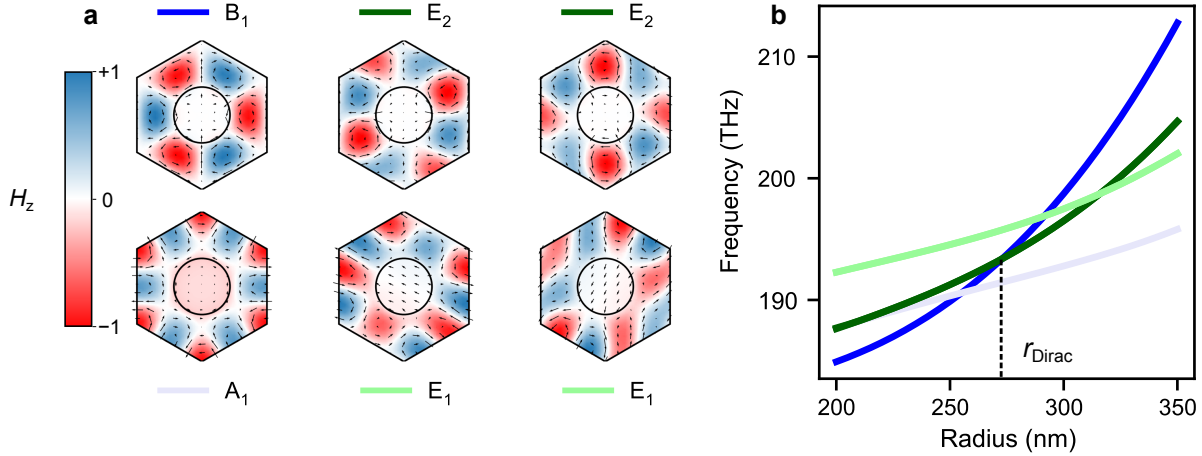

Figure 2.7: *Symmetries of transverse-electric (TE) modes in a photonic crystal and tuning of a Dirac degeneracy.* **(a)** Irreducible representation of the out-of-plane component of the magnetic field H_z at the Γ-point. **(b)** The frequency dependence of the six modes from (a) on the radius of the air holes for a photonic crystal with period $a = 1265$ nm, thickness of $h = 200$ nm, and relative permittivity $\varepsilon = 12$. A Dirac point is obtained when the B_1 mode (dark blue line) intersects the E_2 mode (dark green line) around $r \sim 273$ nm.

We could further use these symmetries to calculate the first-order coupling between any two modes predict the nature of the dispersion when these modes are tuned to a degeneracy. These results presented in Table 2.2 are based on the extensive studies of Sakoda [32, 33]. Finally, noting that the E_1 mode has a non-zero imaginary frequency, the only combination of modes that can maintain Dirac dispersion in a finite structure is the degeneracy between a B_1 or B_2 mode with the E_2 modes (Fig. 2.7b).

Table 2.2: *Dispersion obtained from a degeneracy betweem modes of a* C_{6v} *lattice.*

Mode 1	Mode 2	Dispersion
A_1	B_1, B_2	Quadratic
A_1, A_2	E_1	Dirac
A_1, A_2	E_2	Quadratic
B_1, B_2	E_1	Quadratic
B_1, B_2	**E_2**	**Dirac**
E_1	E_2	Double-Dirac

2.3 Open-Dirac potentials

Now we restrict the periodic potential to a create a cavity such that $V(y) = V_0$ is a constant for $|y| \geq D/2$. The interfaces at $|y| = D/2$ cause the waves inside the cavity to reflect and an interference pattern between the forward- and backward-propagating waves is created. The wavefunction of a cavity mode from the lower band can hence be written as,

$$L_{\Delta,\pm k}(y) = \nu_{\Delta,k}(y)e^{iky} \pm \nu_{\Delta,-k}(y)e^{-iky} \,. \tag{2.44}$$

Note that the solutions for positive and negative wavevector k are exactly the same and we use the sign to indicate whether the cavity mode is even or odd. Substituting Eq. (2.42), we obtain even solutions,

$$L_{\Delta,+k}(y) = u_+(y)\cos(ky) + c_{\Delta,k}u_-(y)\sin(ky) \,, \tag{2.45}$$

and odd solutions,

$$L_{\Delta,-k}(y) = u_+(y)\sin(ky) + c_{\Delta,k}u_-(y)\cos(ky) \,, \tag{2.46}$$

Similar expressions can be obtained for the cavity modes originating from the upper band. When $\Delta \gg k$, $c \to 0$ as is evident from Fig. 2.8a, and the cavity modes resolve to the product of sinusoidal envelopes with the Bloch wavefunctions belonging to the pure bands. This is case for cavities employed in conventional photonic crystal and distributed feedback lasers and the first two modes for each band are shown in Fig. 2.8b,c.

To obtain the magnitude of the wavevector k we need to solve for continuity of the wavefunction and its derivative across the interface. In the region $|y| > D/2$, the constant potential supports propagating or decaying plane wave solutions with β as the propagation constant. Applying the continuity condition at $|y| = D/2$, for the even cavity modes we find,

$$\frac{\partial_y u_+(D/2) + \beta u_+(D/2)}{\partial_y u_-(D/2) + \beta u_-(D/2)} = c_{\Delta,k}\tan(kD/2) \,, \tag{2.47}$$

and for the odd cavity modes,

$$\frac{\partial_y u_+(D/2) + \beta u_+(D/2)}{\partial_y u_-(D/2) + \beta u_-(D/2)} = c_{\Delta,k}\cot(kD/2) \,, \tag{2.48}$$

These are two transcendental equations that can typically be solved only by numerical or graphical methods. However, analytical solutions exist when $\Delta \gg k$ or when $\Delta \ll k$ because in these cases, $c_{\Delta,k}$ can be approximated to be a constant. If $\Delta \gg k$, then $c_l \to 0$. Thus, $\tan(kD/2)$ and $\cot(kD/2)$ need to be large for the boundary conditions to be satisfied. As a result, we obtain $k \sim n\pi/D$ where n is a positive integer and odd n satisifies Eq. (2.47) while even n satisfies Eq. (2.48). A similar arguement can be made for the upper band as $c_u \to \infty$ with the only difference being that odd n yields odd solutions and even n yields
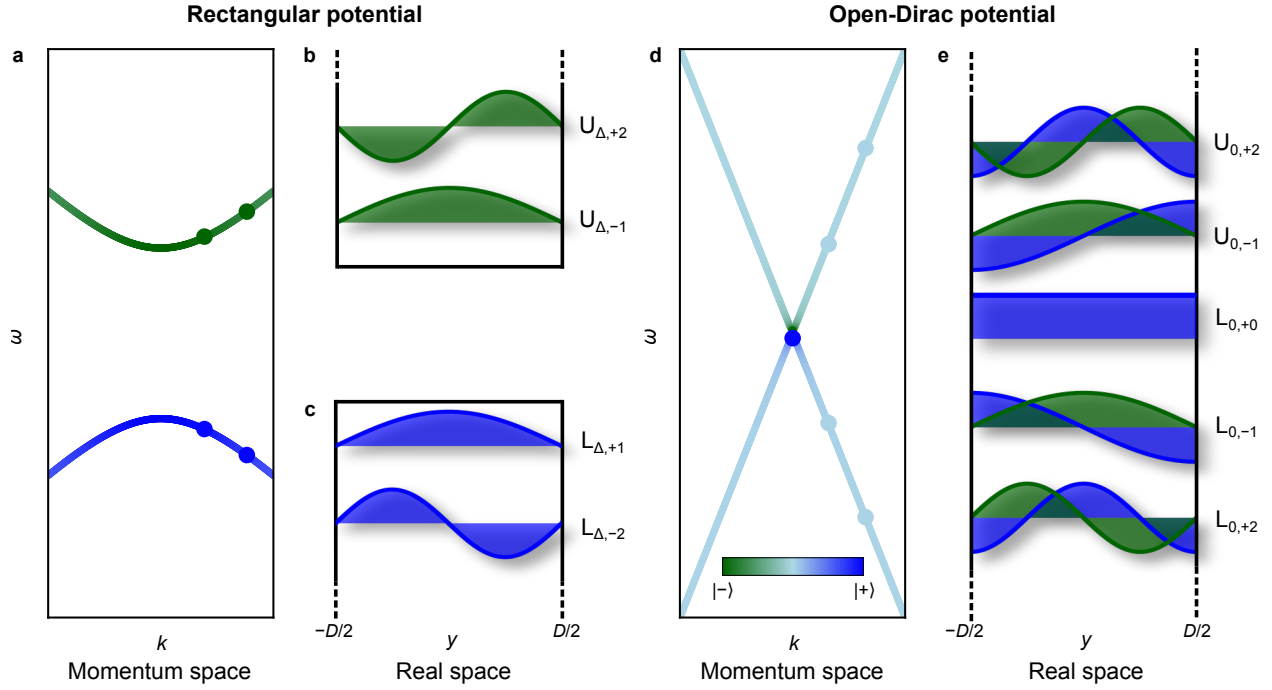
Figure 2.8: *Dispersion and cavity modes for quadratic and open-Dirac potentials.* **(a)** Quadratic band edges when the odd (green) and even (blue) modes are separated by frequancy Δ. **(b,c)** The modes of the two bands originating from both the bands with a quadratic dispersion are similar to conventional modes in a uniform potential well with $k = n\pi/D$ where $n = 1, 2, 3, \ldots$. **(d)** When the frequency separation between the two modes approaches 0 the dispersion turns linear and the bands consist of admixtures from both Bloch modes. **(e)** The cavity modes of an open-Dirac potential with linear dispersion are a mix of both odd and even states with the same k and a $\pi/2$ phase shift.

even solutions. The appropriately labelled cavity modes for the upper and lower bands are shown in Fig. 2.8b,c.

A more interesting situation arises when $\Delta \sim 0$. Let us consider the case when the numerator $\partial_y u_+(D/2) + \beta u_+(D/2) \sim 0$. Now, $c_{\Delta,k} = -1$ and clearly $k \sim 0$ is a solution. Thus, a cavity mode with a flat envelope can exist in such a potential. The higher-order modes still follow the $k \sim n\pi/D$ sequence but the field distribution in the cavity includes contribution from both the odd and the even Bloch modes as shown in Fig. 2.8e.

2.3.1 One-dimensional photonic cavities

A photonic realization of the open-Dirac potential can be obtained based on Table 2.2 and Fig. 2.7b. The odd and even modes are the transverse-electric (TE) Bloch solutions belonging

to the E_2 and B_1 irreducible representations of a C_{6v} lattice. The out-of-plane component of the magnetic field H_z shown in Fig. 2.7a and the inset of Fig. 2.9a can be used to identify these symmetries. In the M-direction (y-direction in the Cartesian system), the green E_2 mode is odd and the B_1 mode is even whereas in the K-direction (x-direction), the orange E_2 is even while the B_1 mode is odd. When the detuning between the modes is large, the dispersion is quadratic (Fig. 2.9a) but when $\Delta \sim 0$ the orange band turns linear in the K-direction and the green band turns linear in the M-direction as shown in Fig. 2.9b.
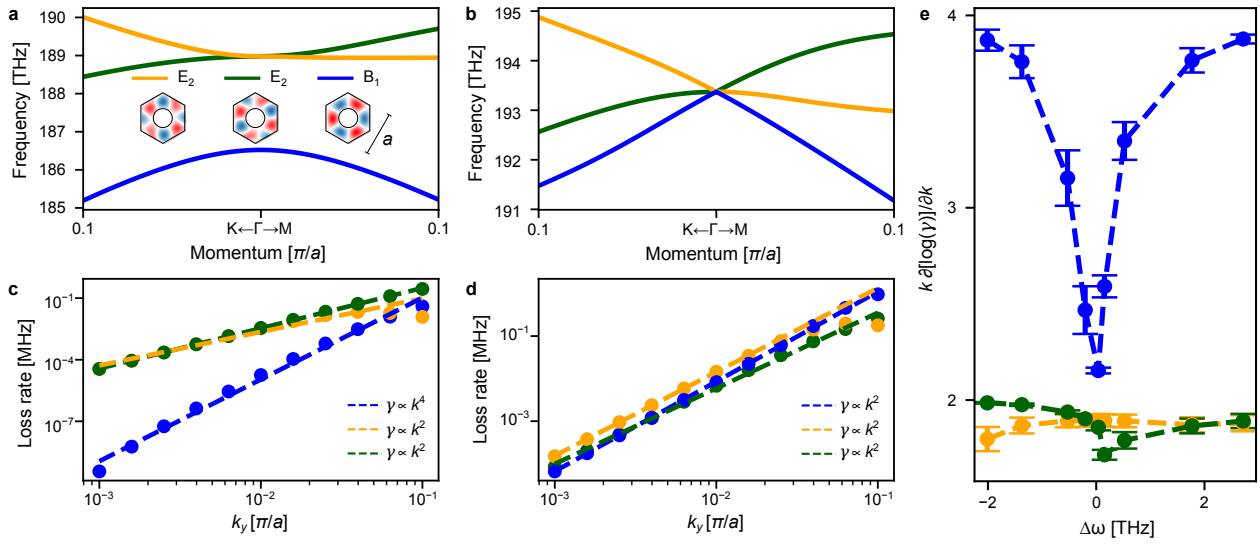
Figure 2.9: *Dispersion and photonic admixtures in open-Dirac potentials.* **(a)** Quadratic dispersion for bands in a photonic crystal when the unit cell modes are non-degenerate. Inset shows the out-of-plane magnetic field distribution. **(b)** The dispersion turns linear as the B_1 and E_2 modes are tuned to a degeneracy. Not that the E_2 couples with the B_1 mode in the M direction whereas the other E_2 mode couples with the B_1 mode in the K direction. **(c)** The scaling of the radiative loss rates of the three modes. The loss of the B_1 mode scales as k^4 and the loss of the E_2 modes scales as k^2. **(d)** Photonic admixtures of the B_1 and E_2 modes causes all three mode to follow a k^2 scaling. **(e)** The slope of the loss rate of the B_1 mode in log scale approaches the same slope as that of the E_2 modes as $\delta \to 0$.

Due to their symmetry, all three modes are topological in nature. These modes do not radiate at the Γ-point and produce a polarization vortex in the far field. The scaling of the loss rates in k-space can can be predicted from the vorticity of the real space field distribution. When the disperion is quadratic, the loss rates of the doubly degenerate E_2 modes scale with the square of the momentum while the loss rate of the B_1 mode has a quartic dependence on k, as can be seen in Fig. 2.9c. However, when the lattice is tuned to a three-fold degeneracy, the B_1 band also contains an equal proportion of the E_2 field distribution as per Eqs. (2.41)

and (2.42) and the k^2 contribution of the loss from the E_2 part dominates. This is seen in Fig. 2.9d as all three lines are nearly parallel with slope ~ 2.

Now the photonic crystal is truncated only along the y-direction while maintaining $k_x = 0$. This causes only the green E_2 mode to couple with the B_1 mode within the cavity. The orange E_2 band remains decoupled and does not participate in cavity modes arising from the linear bands but a very similar analysis holds for this band if the truncation was in the x-direction. A comparison of the loss rates and the wavevector of the cavity modes with the loss rates and dispersion of the infinite system (unit cell) is presented in Fig. 2.10a,b. The loss rates of the cavity modes lie mostly on the green and blue lines obtained from the unit cell but are shifted slightly to the right. This is due to additional radiative losses arising from the boundaries which do not exist in the infinite periodic system. The momentum k for the envelope of the cavity modes follows precisely the pattern expected from Eqs. (2.47) and (2.48). As the position of the boundaries favors a $k_y = 0$ solution for the even mode we obtain an L0,0 mode at the Dirac point in the dispersion. The higher order modes from there on are shifted by $k_y = \pi/D$ along both the bands.
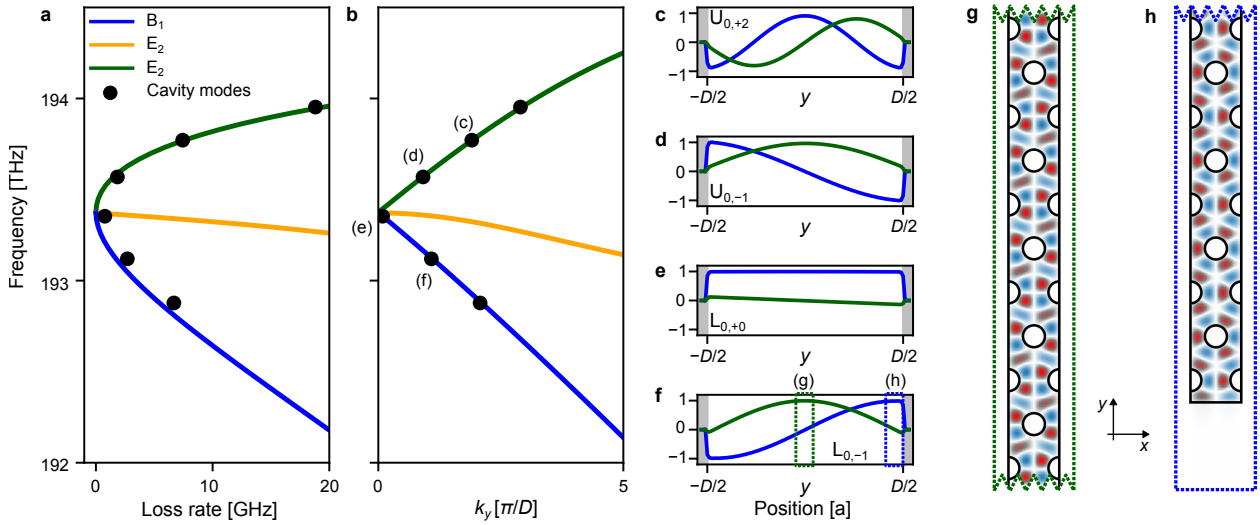

Figure 2.10: *Modes in a photonic open-Dirac cavity.* **(a)** The frequency dependence of the loss rate of the three bands and the cavity modes with cavity size $N = 101a$. **(b)** The frequency of the cavity modes overlayed on the dispersion along the y-direction. **(c,d,e,f)** The distribution of the B_1 and E_2 components across the cavity for the first four lowest order modes. **(g)** A closer look at the center of the cavity for mode $L_{0,-1}$ showing contribution from mainly the E_2 mode. **(h)** The edge of the cavity for $L_{0,-1}$ showing the predominantly B_1 contribution.

The distribution of the B_1 and E_2 modes within the cavity can be visualized by taking the overlap integral of the electromagnetic fields for the Bloch wavefunctions with the corresponding field component in each unit cell of the cavity. The resuls are shown in Fig. 2.10c-f.

For example, the $L_{0,-1}$ mode (Fig. 2.10f) has the field distribution,

$$L_{0,-1}(y) = u_{B_1}(y)\sin(\pi y/D) + u_{E_2}(y)\cos(\pi y/D). \tag{2.49}$$

Hence this mode has an E_2 symmetry in the center of the cavity as seen in Fig. 2.10g. However, if we take a closer look towards the edge of the cavity we find a predominantly B_1 symmetry (Fig. 2.10h).

The wavevector of the envelope for a photonic crystal cavity mode can be computed from the electromagnetic equivalent of Eqs. (2.47) and (2.48). For TE modes, this can be done by replacing the wavefunction with the magnetic field and the derivative of the wavefunction with the electric field component parallel to the interface. The solutions for the envelope wavelength for the electromagnetic boundary condition as a function of the position of the cavity interface are plotted in Fig. 2.11a. When a complete unit cell is present at the boundary, or equivalently, when the interface lies exactly between two rows of air holes, $L_{0,0}$ is the fundamental mode of the cavity (Fig. 2.10e). Moreover, by changing the location of the interface we can control the wavelength of the envelope. As the fraction of the unit cell at the boundary becomes smaller, we find that the wavevector of the lowest order even mode (B_1 dominant) starts increasing while the wavevector of the lowest order odd mode (E_2 dominant) starts to approach zero. This is shown in Fig. 2.11a where the solid lines are obtained by solving the boundary conditions and the dots are obtained by fitting the envelopes extracted from the overlap integral to the cosine function for cavities with the corresponding boundaries.
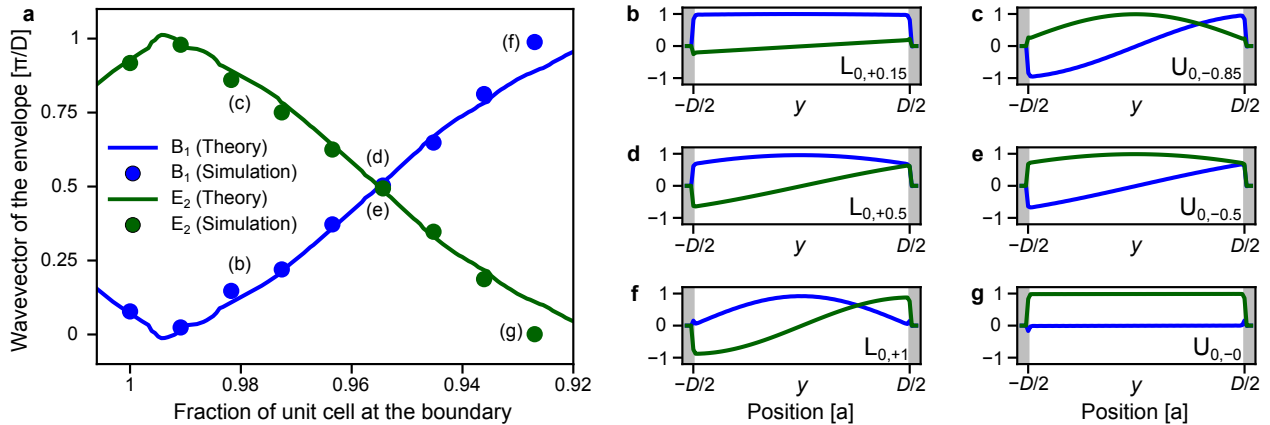

Figure 2.11: *Envelope control in open-Dirac potentials.* **(a)** The wavevector of the envelope for the lowest order modes in an open-Dirac potential. **(b-g)** Distribution of the Bloch wavefunctions within the cavity in a few indicative cases for the lowest order **(b,d,f)** even mode and **(c,e,g)** odd mode.

The envelopes of the cavity modes for a few indicative modes of the open-Dirac cavity as the interface position changes are showin in Fig. 2.11b-g. In Fig. 2.11b,c, the interface

is still located close to the original position. Thus, even as the wavevector increases, the envelope looks relatively flat and $L_{0,0.15}$ is the fundamental mode. The envelope of the odd mode however no longer goes to zero at $\pm D/2$ indicating that the $k < \pi/D$. As more of the unit cell at the boundary is removed, the cavity reaches a point where both the modes hav the same wavevector (Fig. 2.11d,e). Once the fraction of the unit cell at the boundary is ~ 0.92 we find that it is now the odd E_2 mode that uniformly spreads throughout the cavity whereas the envelope of the even B_1 mode has a conventional π/D wavevector. This shows that open-Dirac cavities can also be tuned to control the wavelength of a cavity mode and also the field distribution at the unit cell level.

2.3.2 Photonic admixtures in two-dimensional Fourier space

For a more practical realization, the cavity must be truncated along all three directions. The boundary conditions to rigorously compute the envelope for two-dimensional cavities is not covered here but the same arguments developed in the previous sections can be applied to obtain an intuitive picture. This idea is demonstrated in Fig. 2.12a where the dispersion of the PhC at r_{Dirac} is overlaid on the discrete cavity modes. The colour of these modes indicates the purity of the eigenvector. We observe that when we are close to the Dirac singularity, only the fundamental mode at the Γ-point is purely B_1 as expected from our analysis of one-dimensional cavities. Higher-order modes originating from both the B and E bands consist of an admixture of fields from both these bands. The separation between modes $\delta_k \sim \pi/D$ is still governed by the length of the cavity D and the momentum of the fundamental mode σ_k also obeys the same boundary conditions derived in Eqs. (2.47) and (2.48). The presence of the corners reduces feedback along the K-direction of the Brillouin zone and high-quality-factor (Q) modes are supported only along the M-direction. The five lowest-order modes are computed for a cavity with $D = 51a$ are presented in Fig. 2.12a.

Due to the six-fold symmetry of the cavity and the B_1 mode, satisfying the boundary condition at one edge is sufficient to compute the momentum of the fundamental cavity mode. If we correctly choose the boundaries according to Fig. 2.11, then we can obtain an infinite-wavelength mode even in a two-dimensional cavity. This means that, unlike the fundamental mode of conventional photonic cavities that have a cosine envelope, the fundamental mode in our open-Dirac cavity with hexagonal boundaries has a flat envelope for all cavity sizes. This is confirmed in Fig. 2.12b for open-Dirac cavities of sizes $D = 19a$, $D = 35a$, and $D = 51a$. Such a mode locks all the resonators at of the laser in phase regardless of the size of the cavity and eliminates spatial hole burning by uniformly depleting gain across the cavity.

To better understand the formation and mixing of modes in a two-dimensional cavity, we compare the fields in a hexagonal open-Dirac cavity with another hexagonal cavity detuned from the singularity. The three lowest order modes for a cavity with quadratic dispersion are presented in Fig. 2.13. The fundamental mode (Fig. 2.13b) seems to be spread uniformly as the detuning is not strong enough. The first higher mode from the B_1 band evidently has a sine-like envelope (Fig. 2.13a) and does not show contributions from the E_2 band. This is
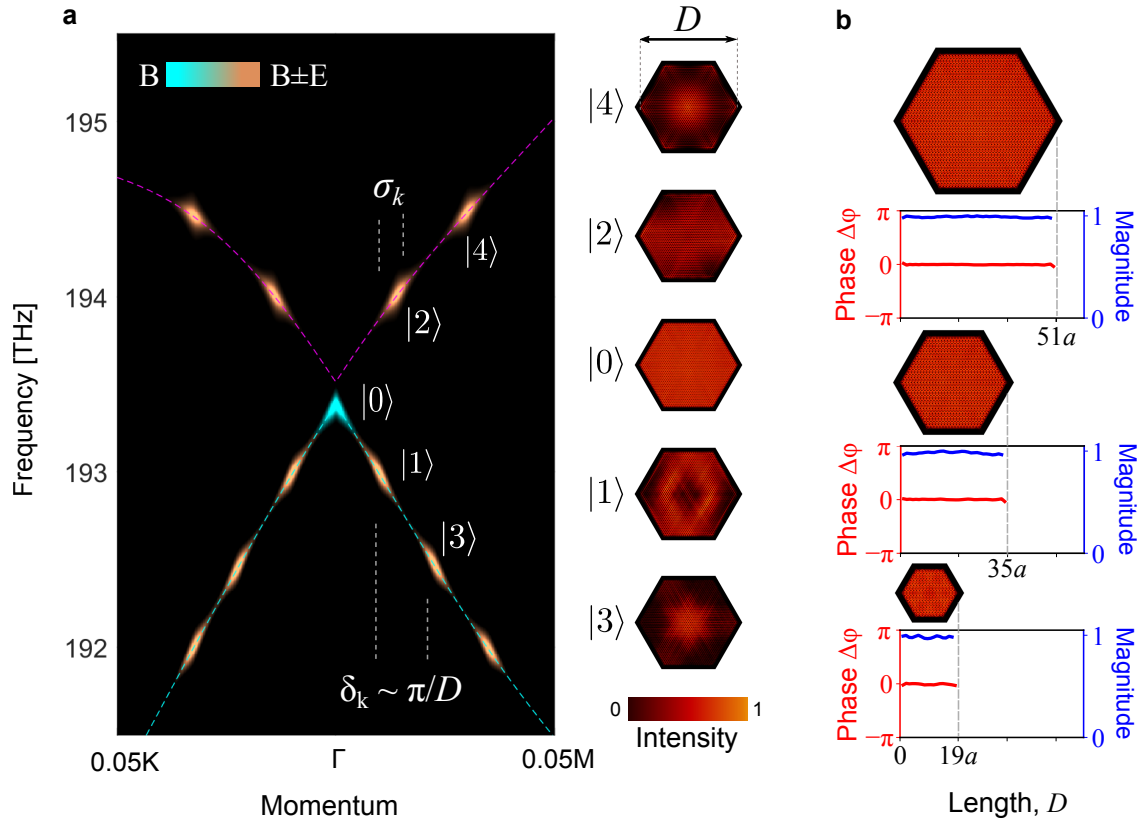
Figure 2.12: *Modes of a hexagonal open-Dirac cavity.* **(a)** Cavity modes on the dispersion of the unit cell (dashed lines), presented in colour to indicate the mixing of the B_1 and E_2 bands. The fundamental mode at the Γ point is the only purely B_1 mode (cyan). Higher-order modes (copper) are photonic admixtures of the B_1 and E_2 bands and thus demonstrate a different scaling than the fundamental mode. The blur around cavity modes indicates the uncertainty in the momentum σk owing to the finite size of the cavity, and the spacing between the modes is the momentum imparted by the cavity δk. The electric-field intensity of the five lowest-order modes for a cavity of size $D = 51a$ (where a is the size of the unit cell) is shown on the right. **(b)** Phase of the out-of-plane component of the magnetic field H_z (sampled at the same point in each unit cell along the diagonal of the cavity) and magnitude of the electric field $|\boldsymbol{E}|$ (averaged over each unit cell along the diagonal of the cavity) for cavities of sizes $D = 19a$, $D = 35a$, and $D = 51a$. The fundamental mode $|0\rangle$ has a flat envelope regardless of cavity size.

not obvious from the real-space field distribution but becomes apparent when we take the Fourier transform of the complex H_z field. The symmetry and patterns seen in Fig. 2.13d,g are very similar to Fig. 2.13e,h. Hence, even though the functional form of the envelope from the E_2 band cavity modea (Fig. 2.13c) is not immediately apparent, we observe a marked difference in the Fourier space distribution (Fig. 2.13f,i). For example, the field in cavity modes from the B_1 band is mainly concentrated at the K-points of the Brillouin zone but in Fig. 2.13f, the M-points are also comparably bright.

The white circle in the Fourier space fields represents the light cone. Field components within this circle can radiate into the far field and the integral within this region can be used to compute the loss rate of the modes. We note that as the E_2 modes are not compatible with the six-fold symmetry of the cavity, we see six "crossings" within the light cone in Fig. 2.13i indicating a higher loss rate than the higher-order mode from the B_1 band.

Now we shift our focus to the cavity modes in the open-Dirac potential. From Fig. 2.14a we can clearly see that the well behaved sine-like envelope is not replaced with a messy interference pattern caused by the contribution of the E_2 component. This is further validated by noting that Fourier space representations of the higher-order modes in Fig. 2.14d,f are very similar. The M-points for both these cavity modes contain significant field components indicating the presence of the E_2 symmetry. Finally, we also note that both higher-order mode also display the six crossing in the light cone in Fig. 2.14g,i and will thus have a much higher loss rate than the fundamental mode (Fig. 2.14h).

In summary, this chapter establishes a foundational framework for understanding and utilizing open-Dirac potentials. We have shown their capacity to manipulate field distributions within photonic crystal slab cavities at both the unit cell level and across the entire cavity. This capability stems from applying standard electromagnetic interface conditions to a photonic admixture of modes, giving rise to unique cavity modes with distinctive properties. These advancements not only deepen our understanding of photonic systems but also open the door to a wide range of applications that necessitate precise control over wave dynamics in various physical contexts. Future research may explore further practical implementations of these principles, paving the way for developing innovative innovative technologies.
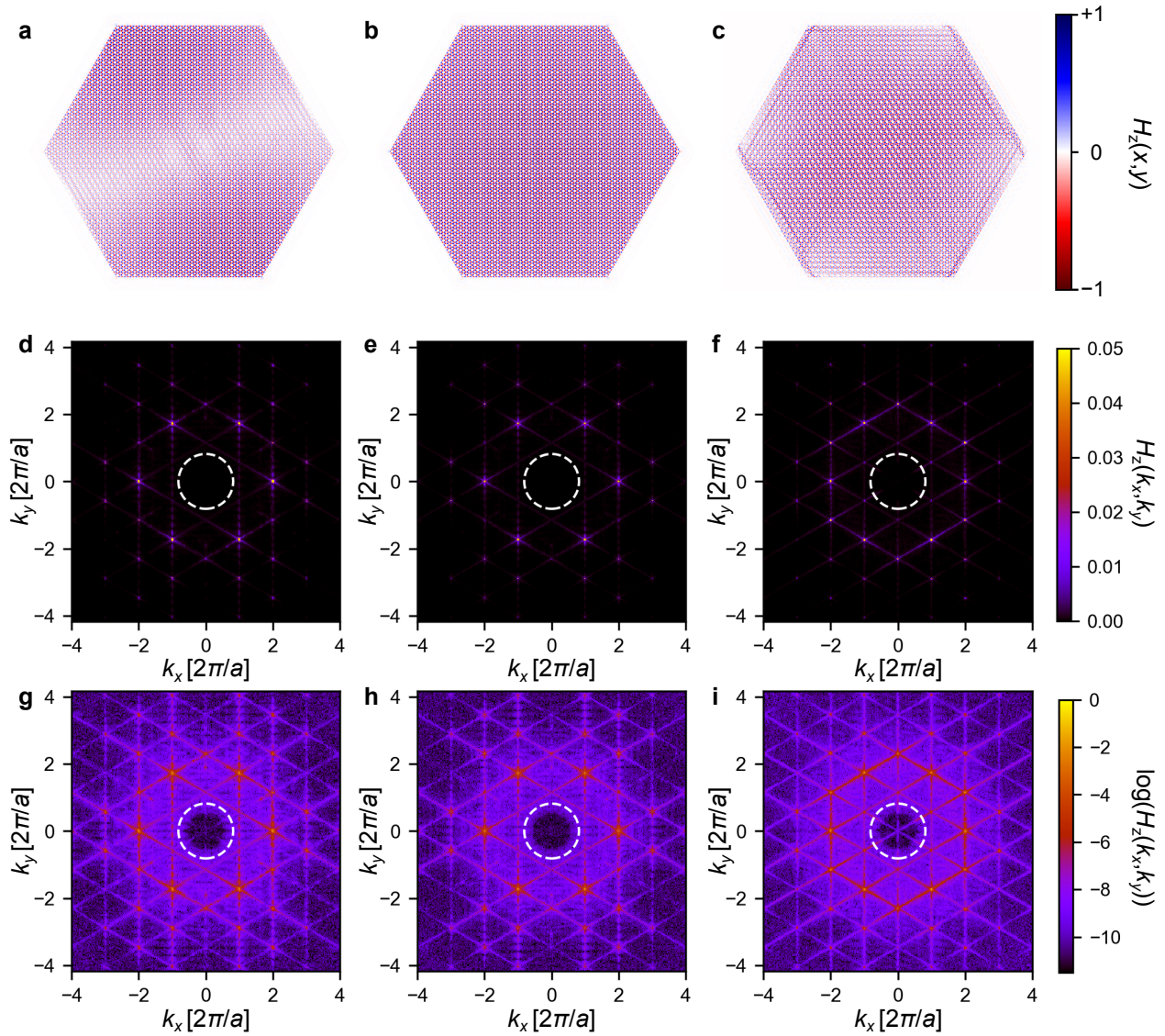
Figure 2.13: *Modes of a conventional hexagonal cavity in real- and Fourier-space.* **(a-c)** Distribution of the out-of-plane component of the magnetic field H_z in real-space for **(a)** the first higher-order mode from the lower band, **(b)** the fundamental mode, and **(c)** the first-order mode from the upper band. **(d-i)** Fourier expansion of H_z in **(d-f)** linear scale and **(g-i)** in log scale for the same three modes as **(a-c)**.
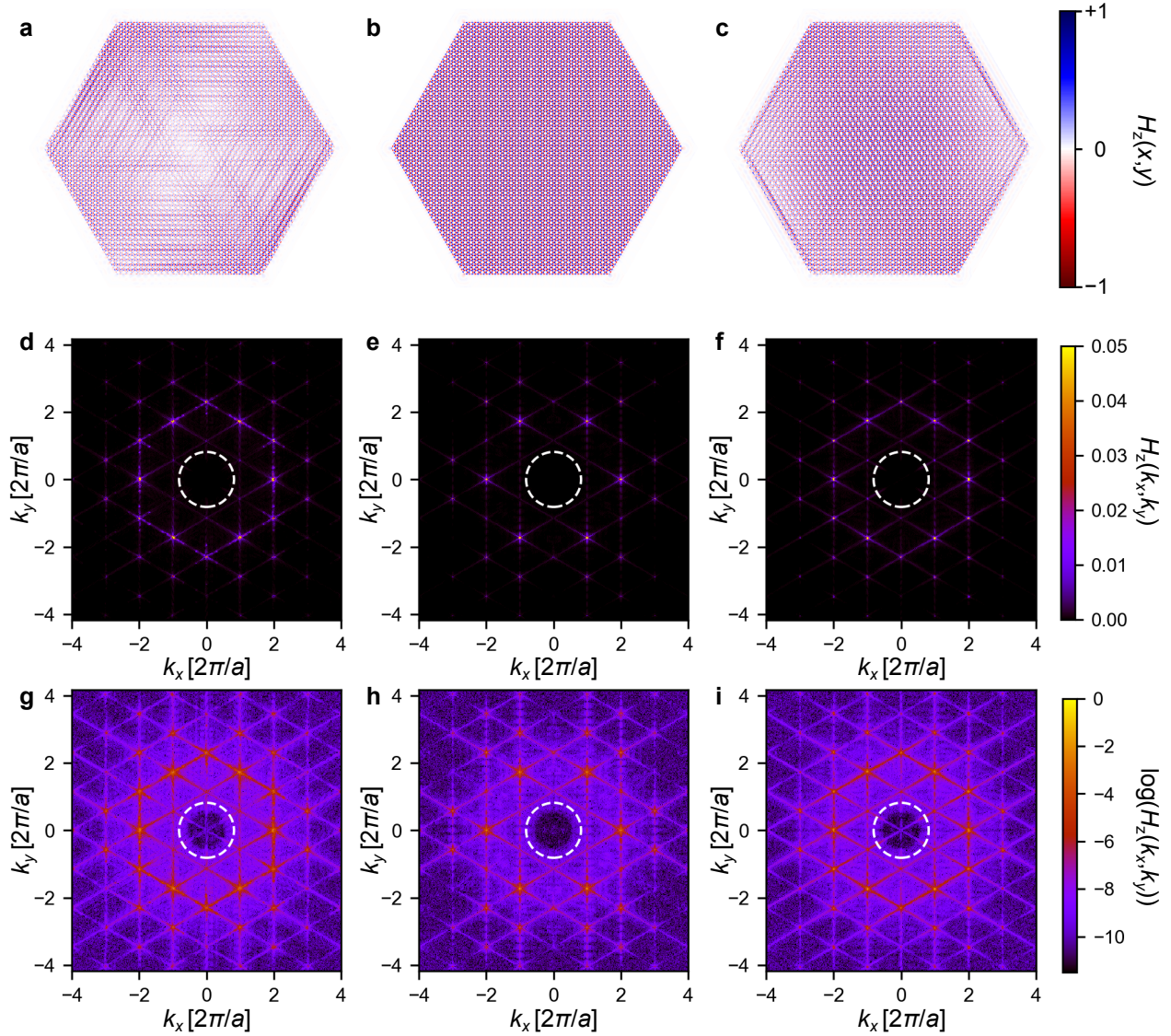
Figure 2.14: *Modes of a hexagonal open-Dirac cavity in real- and Fourier-space.* **(a-c)** Distribution of the out-of-plane component of the magnetic field H_z in real-space for **(a)** the first higher-order mode from the lower band, **(b)** the fundamental mode, and **(c)** the first-order mode from the upper band. **(d-i)** Fourier expansion of H_z in **(d-f)** linear scale and **(g-i)** in log scale for the same three modes as **(a-c)**.

Chapter 3

The Berkeley surface-emitting laser

The quest to scale up laser cavities while maintaining single-mode operation has been a longstanding challenge since the laser's inception over sixty years ago [1, 42–48]. This challenge is particularly pronounced in single-aperture cavities, crucial for emitting a coherent beam of light. However, the emergence of higher-order transverse modes with increasing cavity size has been a persistent obstacle. This chapter introduces a novel approach to this problem: the Berkeley surface-emitting laser (BerkSEL). An overview of a BerkSEL in operation is presented in Fig. 3.1a. The suspended hexagonal open-Dirac cavity is supported by six bridges and the linear dispersion in two-dimensional momentum space is depicted in Fig. 3.1b.

While recent theoretical proposals have suggested using a three-dimensional structure to implement a Dirac cone for large-area single-mode lasing, these have relied on separation in the real part of the frequency spacing of cavity modes [49, 50]. Such changes are typically smaller than the gain bandwidth of semiconductors, proving inadequate for ensuring single-mode operation in lasers. Additionally, these models often result in modes with non-uniform wavefunctions, presenting further limitations. Here, we will explore how the open-Dirac electromagnetic cavities, featuring linear dispersion realized by a truncated photonic crystal in a hexagonal arrangement, exhibit an unconventional scaling of losses. This phenomenon leads to single-mode lasing that persists as the cavity size increases. The open-Dirac cavity's unique flat-envelope fundamental mode ensures in-phase locking of all unit cells within the cavity, facilitating single-mode lasing.

3.1   Scaling of open-Dirac cavities

In Section 2.3, we derived the dispersion of the complex frequency for an infinite system. To include the effects of finiteness and boundaries of the cavity, we introduce a "finite -size"
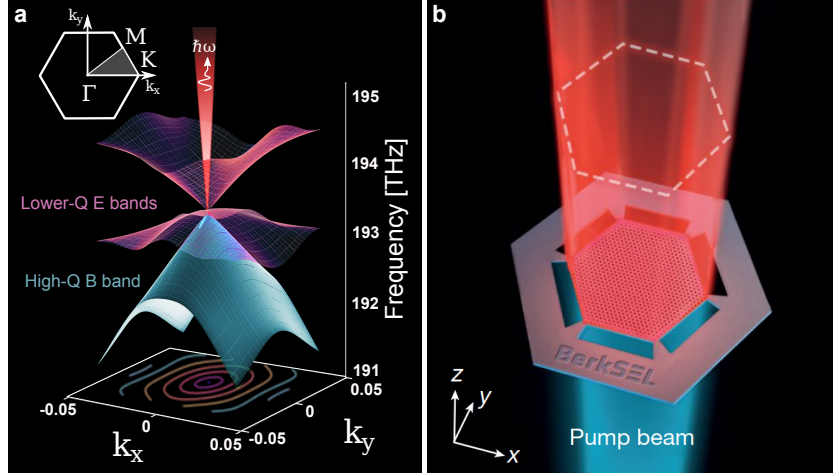
Figure 3.1: *Artistic representation of the BerkSEL.* **(a)** Dispersion of a hexagonal open-Dirac cavity showing a conical degeneracy tuned to 193.5 THz. The blue sheet corresponds to the frequency of the B_1 mode and the red sheets correspond to the E_2 modes. The truncation of the crystal is notably chosen to be more favourable for the B mode compared with the E modes. The iso-frequency contours, projected on the (k_x, k_y) plane, are sketched together with a representation of laser emission originating from the Dirac point. $\hbar$ is the reduced Planck constant and ω is the angular frequency. The inset shows the Brillouin zone for a C_{6v} lattice. **(b)** Schematic of a Berkeley surface-emitting laser (BerkSEL) illustrating the pump beam (blue) and the lasing beam (red) from an open-Dirac cavity mode that admits an infinite-wavelength mode with a uniform field distribution across every unit cell. Therefore, all unit cells (or resonators) in the cavity are synchronized in phase and contribute to the lasing mode.

operator $\mathcal{F}$ such that,

$$\hat{\mathcal{F}} \begin{pmatrix} |\text{B}\rangle \\ |\text{E}_+\rangle \\ |\text{E}_\times\rangle \end{pmatrix} = \mathbf{\Omega} \begin{pmatrix} |0_u\rangle \\ |0_l\rangle \\ |1_u\rangle \\ |1_l\rangle \\ \vdots \end{pmatrix} . \tag{3.1}$$

This operator transforms the unit-cell modes of an infinite system into the modes of an open and finite cavity. Here, $\mathbf{\Omega}$ is a diagonal matrix containing the complex eigenfrequencies of the modes of the finite cavity. These cavity modes are denoted by $|n_b\rangle$ for the n-th mode originating from the band b. This operator includes effects from additional loss terms as well as the momentum of the cavity modes computed from Eqs. (2.47) and (2.48). The exact form of the operator would depend on the size, shape, and position of boundaries in the finite cavity and makes for an interesting problem to focus on: Can an operator like this be

mathermatically represented?

This is not a trivial problem to solve but based on the intuition we developed, we can express the coupling between the three lowest order modes as,

$$
\begin{pmatrix} -\beta\sigma_k & 0 & 0 \\ 0 & 0 & \beta\Delta_k \\ 0 & \beta\Delta_k & \delta \end{pmatrix} \begin{pmatrix} |0_B\rangle \\ |1_B\rangle \\ |1_E\rangle \end{pmatrix} = \tilde{\omega} \begin{pmatrix} |0_l\rangle \\ |1_u\rangle \\ |1_l\rangle \end{pmatrix} , \tag{3.2}
$$

where, σ_k is the momentum of the fundamental cavity mode and the momentum of the higher order modes is $\Delta_k \sim \pi/D$. We have assumed prior knowledge that the hexagonal cavity supports a fundamental mode only from the B_2 symmetry. The other two rows of the equation represents the coupling between an isolated cavity mode from the B_1 band at momentum Δ_k with an idolated cavity mode from the E_2 band at the same k-vector.
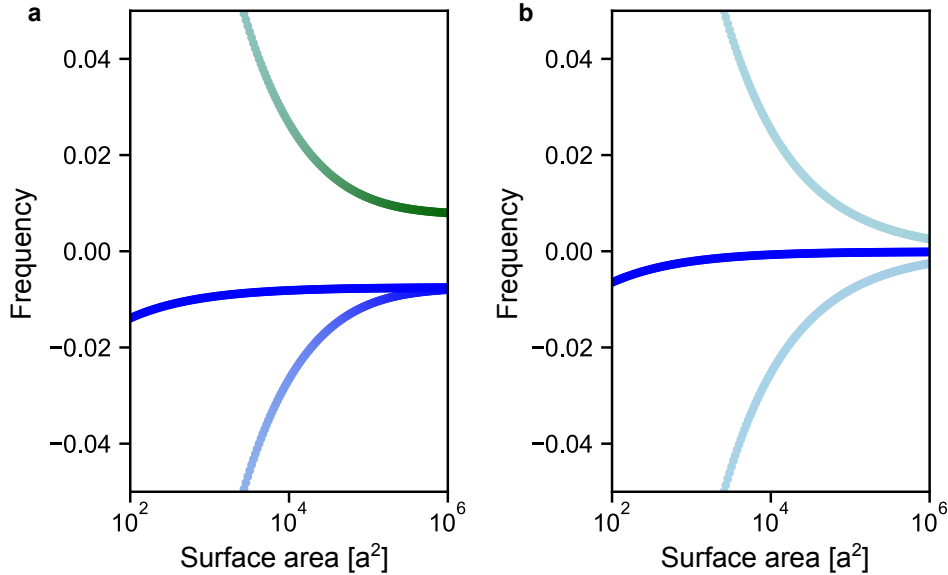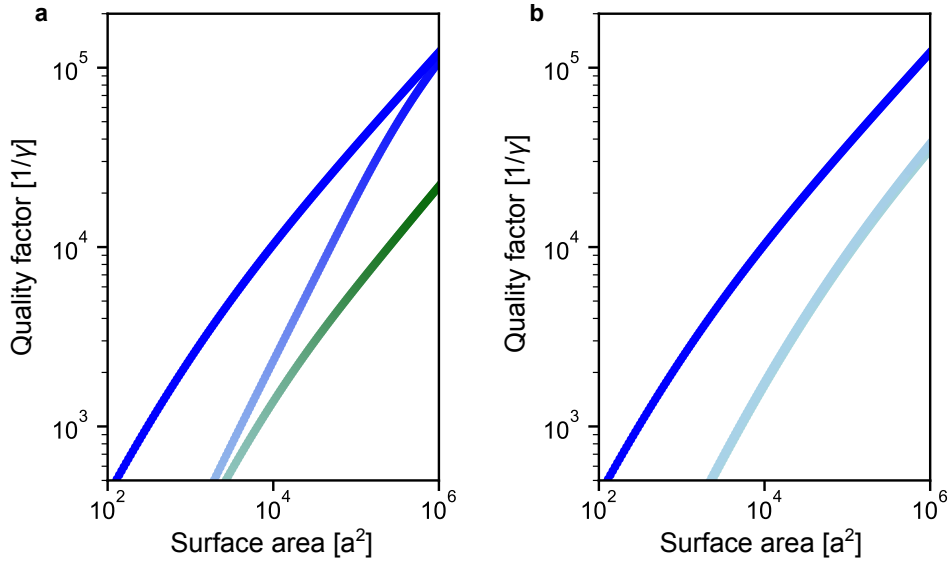

Figure 3.2: *Theoretical scaling of the frequency for the modes in a conventional and open-Dirac hexagonal cavity.* **(a)** The frequency of the higher-order mode from the lower band rapidly approaches the frequency of the fundamental mode. The mixing of symmetries in the higher-order modes disappears as the size of the cavity increases. **(b)** For an open-Dirac cavity, the frequency separation between the fundamental and higher-order modes drops at slower rate than a conventional cavity. The admixture in higher-order modes is also maintained even as the cavity size increases.

Next, we introduce loss into our model. We noticed in Fig. 2.10a that the boundaries introduce some form of radiative loss. So we expect that for an infinitely large structure, the loss rate are only dictated by the topological charge obtained from the winding of the field

distribution. The updated model now looks like,

$$
\begin{pmatrix} -\beta\sigma_k + j\gamma_B & 0 & 0 \\ 0 & j\gamma_B & \beta\Delta_k \\ 0 & \beta\Delta_k & \delta + j\gamma_E \end{pmatrix} \begin{pmatrix} |0_B\rangle \\ |1_B\rangle \\ |1_E\rangle \end{pmatrix} = \tilde{\omega} \begin{pmatrix} |0_l\rangle \\ |1_u\rangle \\ |1_l\rangle \end{pmatrix} ,
\tag{3.3}
$$

where the loss rates can be estimated from the Laurent series as,

$$
\gamma_m = \frac{c_m}{D} + \frac{d_m}{D^2} \quad (m = \text{B, E}).
\tag{3.4}
$$

Figure 3.3: *Theoretical scaling of the quality factor for the modes in a conventional and open-Dirac hexagonal cavity.* **(a)** The quality factor of the higher-order mode from the lower band rapidly approaches the frequency of the fundamental mode. This, along with the dominant B_1 symmetry of the the higher-order mode makes it difficult to separate from the fundamental mode. **(b)** For an open-Dirac cavity, the quality factor separation between the fundamental and higher-order modes maintains a constant ratio determined by the loss rate difference of the B_1 and E_2 symmetries. This helps maintain a strong selectivity for the fundamental mode even as the cavity size increases.

3.1.1 Large-area simulations

To demonstrate the validity of this model, we computed the modes of open-Dirac cavities of different sizes and for hole radii (r) smaller than, equal to and greater than the critical

radius r_{Dirac}. The computation was performed using a three-dimensional finite-element solver for the transverse-electric polarization, which corresponds to the polarization providing the highest gain for the multiple quantum wells used in our work. COMSOL Multiphysics was used to compute the eigenmodes of the cavity surrounded by 2.5 µm of air before the scattering boundaries in the x, y, and $+z$ direction. This is depicted in Fig. 3.4a. To filter out the tranverse-magnetic modes, a perfect magnetic conductor boundary condition was used to mirror half the cavity in the z-direction. This forces the in-plane components of the magnetic to vanish in the center of the cavity and only TE modes are obtained.
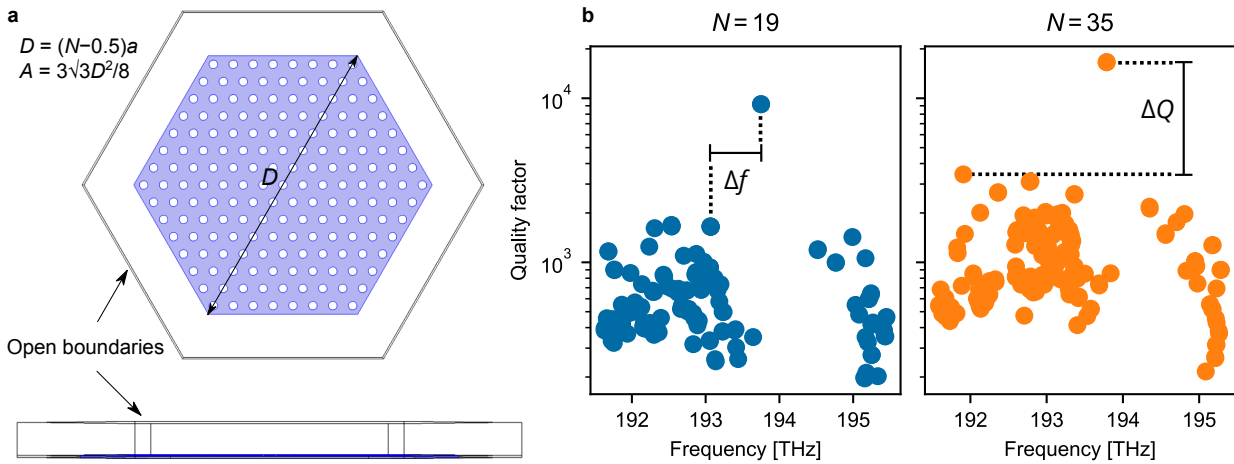

Figure 3.4: *Simulation of finite-size hexagonal open-Dirac cavities.* **(a)** Simulation domain for finite-element analysis of photonic crystal cavities. The xy-directions have open boundaries conditions to allow radiation into the environment and so does the top boundary in the z-direction. The bottom boundary is set as a perfect magnetic conductor to set the in-plane components of the magnetic field to zero and only allow transverse-electric (TE) modes. **(b)** Plots of the raw data from the complex eigenfrequencies returned by the solver. The quality factor is computed as $Q = f/(2\gamma)$, where f is the real-part and γ is the imaginary-part of the eigenfrequency.

The solutions are returned as a set of complex eigenfrequencies and the corresponding field distributions. The eigenfrequencies can be converted to the quality factor as $Q = \omega/(4\pi\gamma)$ and the frequency vs quality factor for two such cavities are presented in Fig. 3.4b. Along with the field distribution within the cavity that was already discussed in the Section 2.3, we can also apply the Stratton-Chu equation to compute the field distribution in the far field. This can be used to visualize the beam profile of a laser operating on the mode under investigation. Figure 3.5 demonstrates how as the cavity size increases, the flat envelope is maintained and the divergence of the beam in the far field becomes narrower.
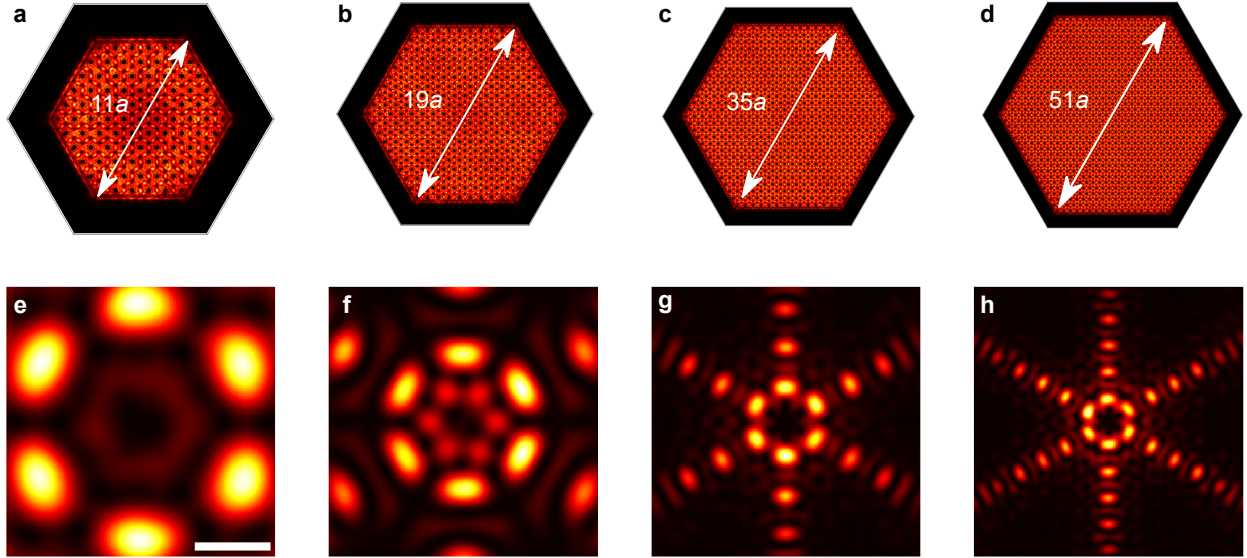
Figure 3.5: *Simulated near field and far field intensity distributions for hexagonal open-Dirac cavities of varying size.* **(a-d)** Near field intensity distribution for **(a)** $D = 11a$, **(b)** $D = 19a$, **(c)** $D = 35a$, and **(d)** $D = 51a$. **(e-h)** Far field beam profile for **(e)** $D = 11a$, **(f)** $D = 19a$, **(g)** $D = 35a$, and **(h)** $D = 51a$. Scale bar equals $10°$.

The results over many such simulations with varying cavity sizes and radii of the air holes are then compiled. Figure 3.6a–c (markers) presents the computed frequency shifts of the first three cavity modes. The frequency shifts are computed by comparing cavity modes to the frequency of the B mode at the Γ point for an infinite membrane with holes of the same radius. Figure 3.6d–f (markers)shows the scaling of Q of the same three modes with increasing cavity sizes. The solid lines are obtained by fitting the simulation data with Eq. (3.3). When the radius of the holes is not close to r_{Dirac}, cavity mode asymptotes to the frequency of the fundamental mode at a rate of D^{-2}. This is shown in Fig. 3.6g along with the scaling for r_{Dirac}, in which case the separation increases and scales at a rate of D^{-1}. It is noted that cavity mode flips from being at a lower frequency than the fundamental mode for $r < r_{\text{Dirac}}$ to a greater frequency than the fundamental mode for $r > r_{\text{Dirac}}$. We also observe that even for the cavity with linear dispersion, the frequency separation rapidly drops to about a terahertz when the diameter of the aperture reaches D = 31a (Supplementary Information). The gain spectrum of semiconductors and notably the quantum wells on which the devices were fabricated, spans almost 100 THz, which is much larger than real mode spacing. The selectivity of the lasing mode can thus not be enabled by the scaling of the frequency shift afforded by linear dispersion alone as initially claimed [49–51].
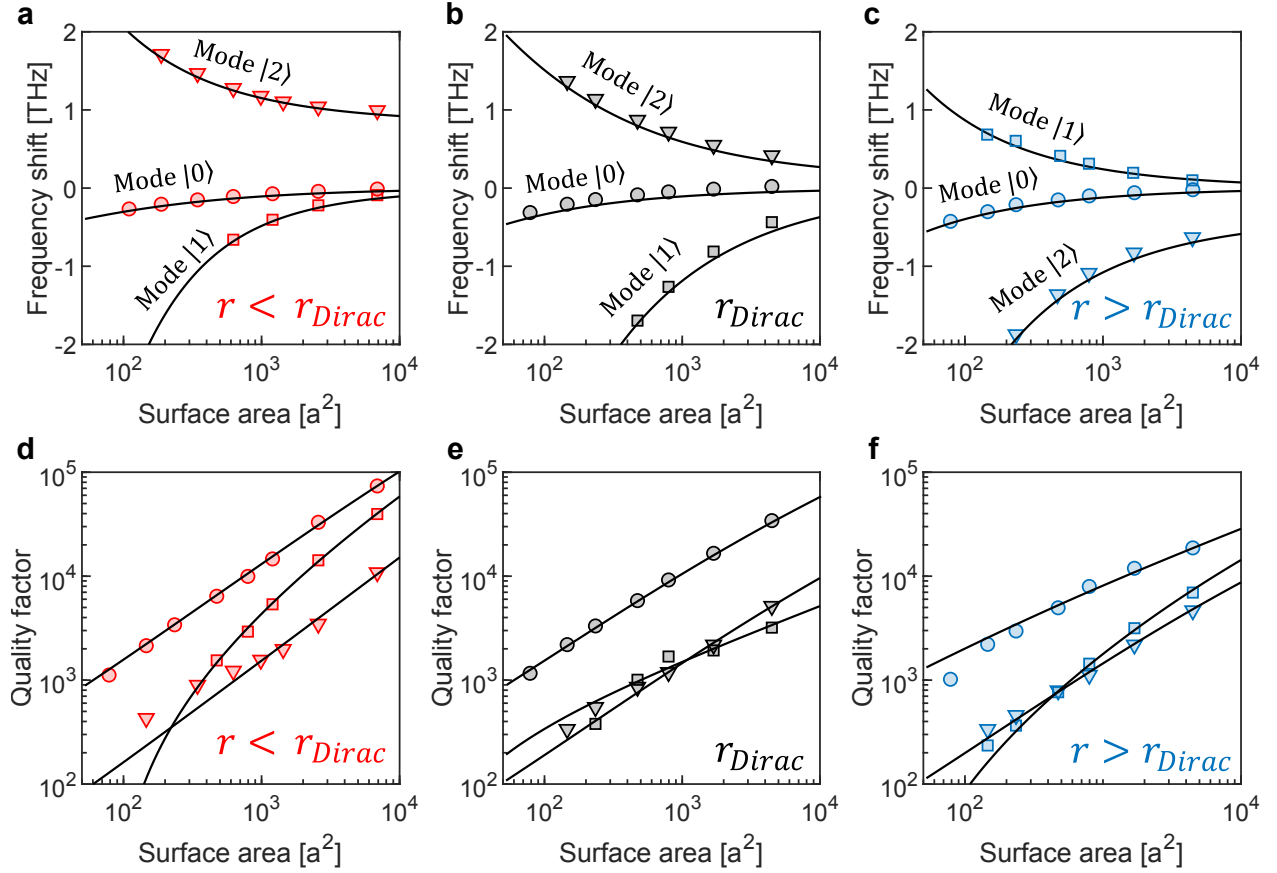
Figure 3.6: **(a–c)** Frequency shifts of the first three cavity modes for **(a)** $r < r_{\mathrm{Dirac}}$, **(b)** $r \sim r_{\mathrm{Dirac}}$, and **(c)** $r > r_{\mathrm{Dirac}}$, computed by comparing cavity modes to the frequency of the B mode at the Γ point for an infinite membrane with holes of the same radius. **(d–f)**, Quality factor of the first three cavity modes for **(d)** $r < r_{\mathrm{Dirac}}$, **(e)** $r \sim r_{\mathrm{Dirac}}$, **(f)** and $r > r_{\mathrm{Dirac}}$. For all plots, the markers are numerical simulations and the continuous lines are theory based on our model.

We now investigate Q of our proposed open-Dirac cavities, with a hexagonal truncation. As previously discussed, the truncation of the cavity serves as selector of the fundamental mode , shown by circles on solid lines in Fig. 3.6. Cavity mode and cavity mode are denoted by square and triangle markers, respectively in Fig. 3.6a–f. Figure 3d–f (markers) shows that, as expected, Q of all the modes increases with the size. We also observe that Q of the fundamental mode (Q0) decreases as the radius of the air-holes increases. This can be attributed to a decrease in the average refractive index of the membrane, which reduces the confinement of light. Analogous to the scaling of frequency, we observe that Q of cavity mode asymptotes to Q0 when r is detuned from r_{Dirac} (Fig. 3.6d ($r < r_{\mathrm{Dirac}}$) and Fig. 3.6f ($r > r_{\mathrm{Dirac}}$)). Surprisingly, when cavities are tuned to the Dirac point ($r \sim r_{\mathrm{Dirac}}$) higher-
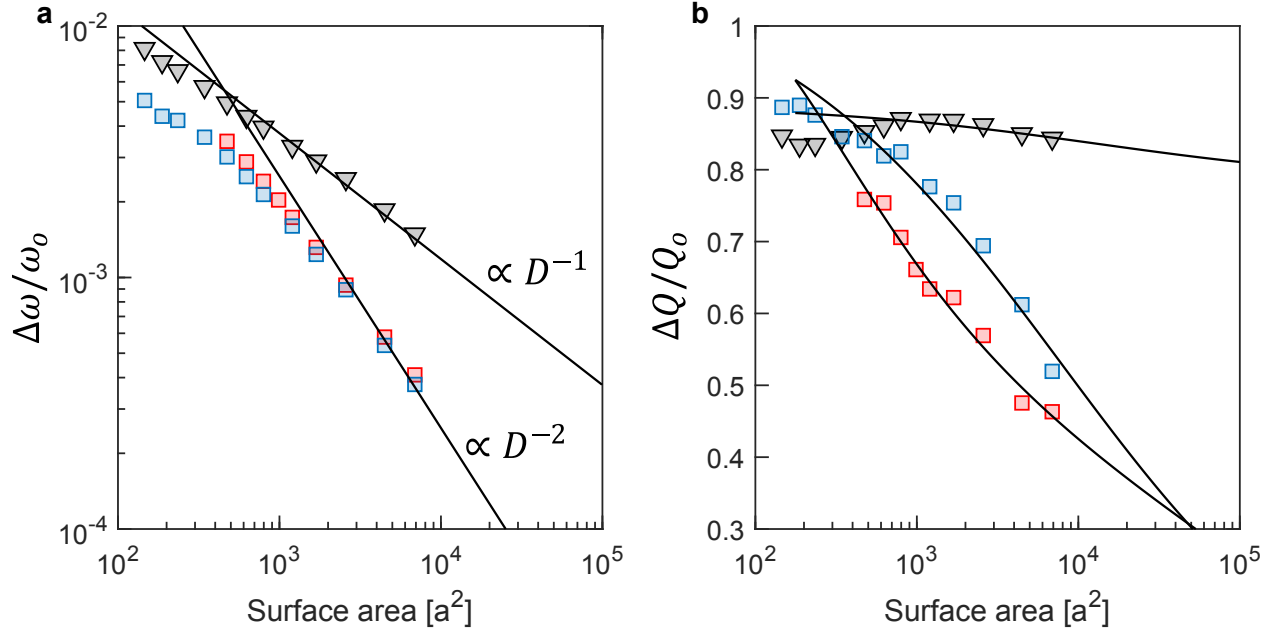
Figure 3.7: *Scaling of frequency and quality factor (Q) separation between the fundamental and higher-order modes.* **(a)** Scaling of the normalized frequency separation as a function of surface-area for cavities with different radii. When the radius is detuned from r_{Dirac}, the dispersion is quadratic, and the frequency shift scales as D^{-2}. When the radius is tuned to r_{Dirac}, the frequency shift scales as D^{-1}. **(b)** Scaling of the normalized difference in Q when the radius is detuned from r_{Dirac} and when it is tuned to the singularity.

order modes do not asymptote to the fundamental mode anymore, as seen in Fig. 3.6e. They lose energy at a rate always higher than the fundamental mode. Unlike the normalized real free spectral range that still decays quickly with the size (Fig. 3.6g), the normalized imaginary free spectral range maintains a non-decaying value despite increasing cavity sizes (Fig. 3.6h). The loss rates of the modes scale with the size of the cavity as (Supplementary Information), where i = B or E, and ci and di are loss rates introduced owing to effects of the boundaries. As the C6 symmetry of the cavity is more favourable for the B band, we find that dE > dB and cE > cB. Moreover, as cavity modes and are formed from an admixture of both the B and the E modes, when $\varepsilon \to 0$ their loss rate is dominated by γE. Hence, for $D \to \infty$, the normalized complex free spectral range tends towards a non-vanishing value of . Theoretical results, plotted in Fig. 3.6a–h as continuous lines, are in perfect agreement with numerical simulations (markers). The imaginary free spectral range in open-Dirac cavities is thus scale invariant. According to the Bloch theorem, cavity modes are the product of the envelopes and unit-cell wavefunctions. The flat-envelope fundamental mode (Fig. 2.12) and the non-vanishing complex free spectral range (Fig. 3.6) prevent cavity-scale and unit-cell-scale spatial hole burnings, respectively. Mixed higher-order modes means that the

cross-saturation is comparable to the self-saturation [52]. Single-mode operation is thus guaranteed for scaled-up surface-emitting lasers operated around open-Dirac singularities (Supplementary Information).

3.2 Fabrication and characterization

The process flow of the nanofabrication is summarized in Fig. 3.8. The photonic crystal cavity is prepared on InGaAsP multiple quantum wells (MQWs) with a gain spectrum over telecommunication wavelength. After the InP capping layer is removed, the InGaAsP wafer is cleaned by typical acetone and isopropyl alcohol ultrasonication. Subsequently, hydrogen
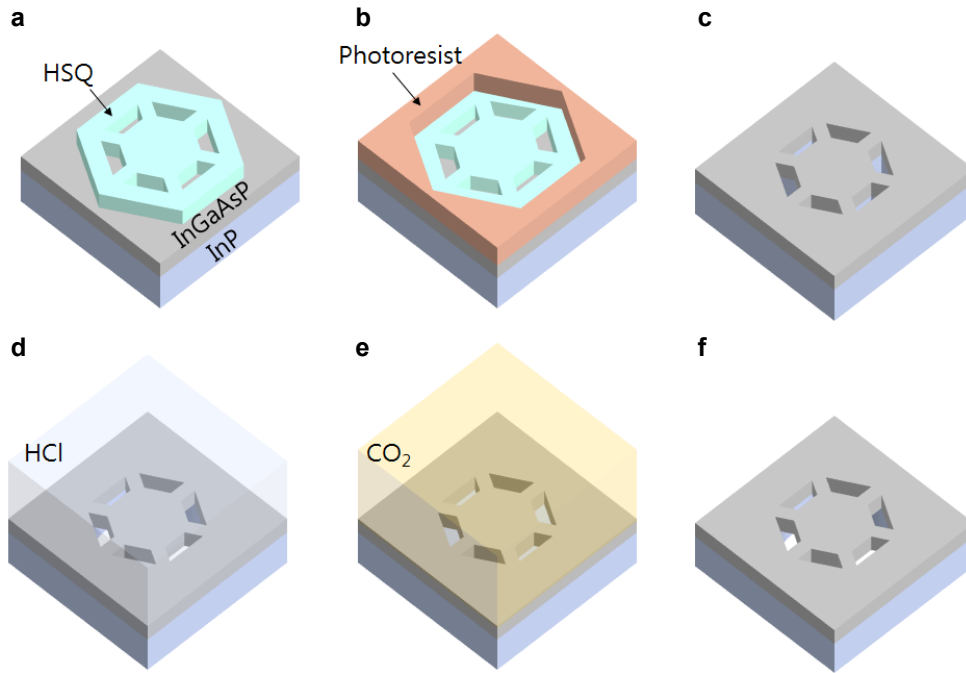

Figure 3.8: *Summary of fabrication steps for a large-scale suspended open-Dirac photonic crystal cavities.* **(a)** Electron-beam lithography to define the photonic crystal. **(b)** Photolithography to protect sacrificial InP layer. **(c)** Dry etching and resist removal. **(d)** Wet etching of InP sacrificial layer under the photonic crystal slab using HCl solution. **(e)** Critical point drying method to avoid stiction of suspended slabs. **(f)** Suspended photonic crystal slab.

silsesquioxane (HSQ) negative tone resist is spin-coated on the wafer and the photonic crystal is patterned by electron-beam lithography [Fig. 3.8a]. To avoid unwanted wet etching of the InP sacrificial layer, we added photolithography [Fig. 3.8b]. In the following step, inductively

coupled plasma (ICP) dry etching with a mixture of H2, CH4, Ar, and Cl2 gas is performed to transfer the patterns to the InGaAsP slab. Then the HSQ layer is removed by a buffered oxide etchant (BOE) solution [Fig. 3.8c]. The device is suspended by a diluted HCl (3:1) solution which selectively removes the InP sacrificial layer under the InGaAsP [Fig. 3.8d]. To avoid stiction issues induced by the capillary force when drying the sample, we introduced the critical point drying (CPD) technique [Fig. 3.8e]. Especially for devices larger than 35 unit-cells, it is critical to eliminate surface tension associated with the drying of a liquid by avoiding the phase transition boundary from liquid to gas. IPA was used as an exchanging solvent, and the supercritical phase of carbon dioxide (CO2) is obtained at the pressure of 1350 psi and a temperature of 31°C. The sample is finalized after supercritical phase carbon dioxide drying [Fig. 3.8f]. Scanning electron microscope images of the finished fabrication process are presented in Fig. 3.9.
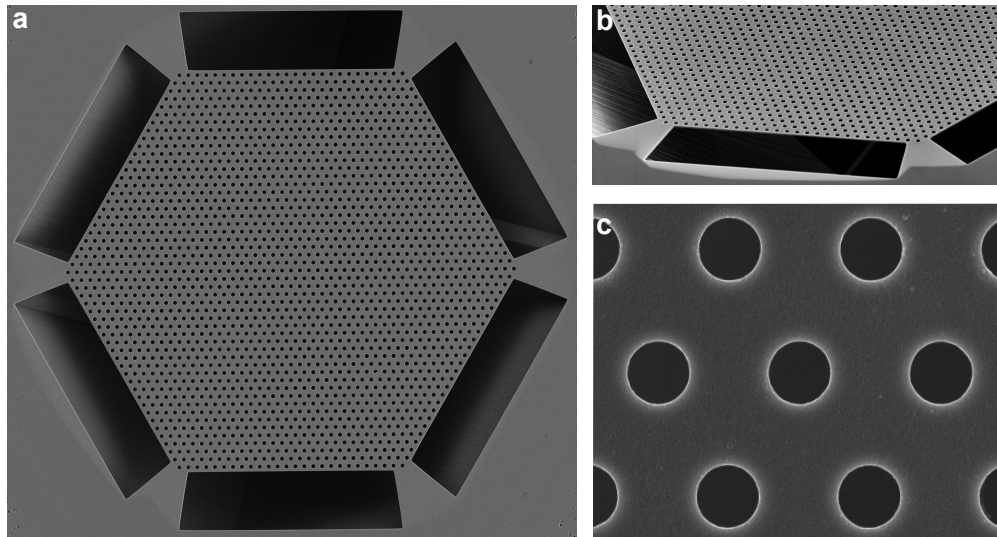

Figure 3.9: *Electron microscope image of a 51-unit cell BerkSEL.* **(a)** Top view showing the suspended photonic crystal membrane supported by six bridges. **(b)** Tilted view focusing on a pair of bridges verifying the undercut required to achieve suspension. **(c)** Zoomed-in view of the unit cell.

The fabricated devices are characterized by photoluminescence (PL) measurements. The PL setup is presented in Fig. 3.10. The sample is optically pumped from the top side with a 1064 nm pulsed laser (12 ns of pulse width and repetition rate of 215 kHz). A 20x long working distance microscope objective (NA of 0.4) focuses the pump beam on the sample and collects the lasing emission simultaneously. The pump beam size is adjusted by a telescope (lenses L1 and L2) tuning the divergence of the beam. The pump power is finely tuned by an optical attenuator and monitored by a power meter. PL signals are captured by an IR-CCD and a monochromator. The spectrum is obtained in conjunction with a cooled

InGaAs detector in lock-in detection configuration. To get a Fourier image of the aperture we image the back focal plane of the objective lens. For autocorrelation measurements we used an Hanbury-brown and Twiss interferometer consisting of a fiber-coupler to direct the signal into a fiber beam splitter. Each end of the beam splitter is connected to two superconducting nanowire single photon detectors. The coincidence histogram is recorded via a time controller.
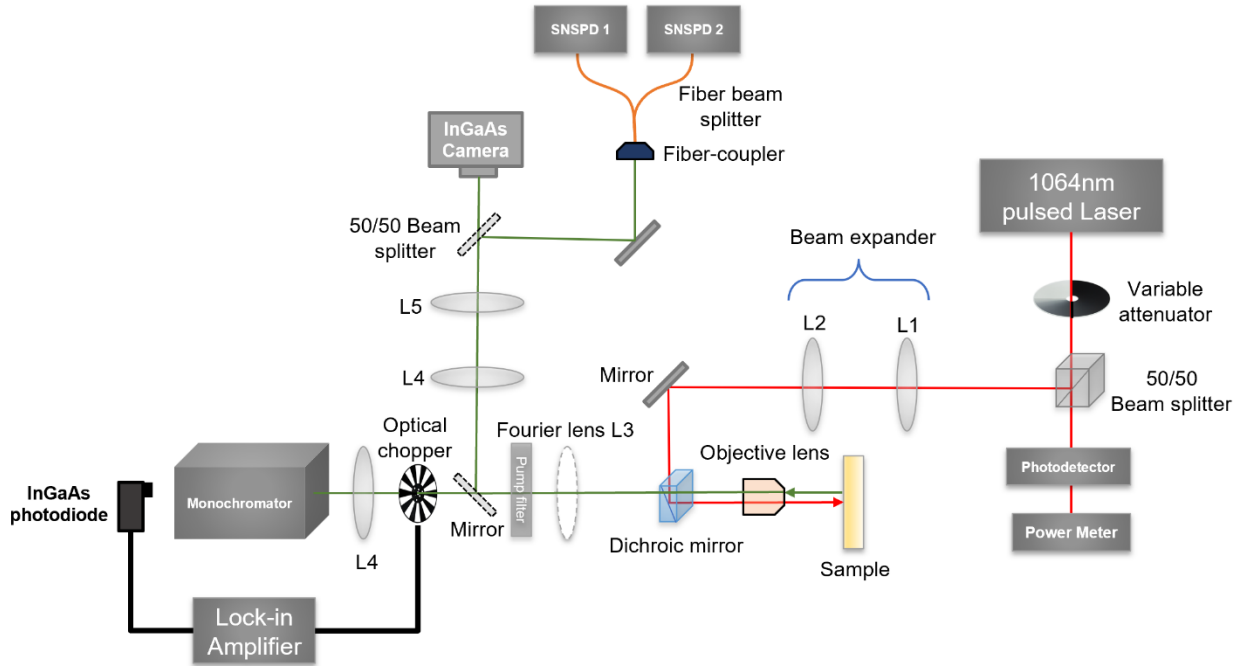

Figure 3.10: *Micro-photoluminescence for laser characterization.*

The measured PL spectrum as a function of the pump power as well as the images of device and its far field under both spontaneous and stimulated emission are depicted in Fig. 3.11.

3.3 Results

To experimentally demonstrate our theory, we characterized Berkeley surface-emitting lasers (BerkSELs) of diameter D = 19a (Fig. 3.12a), D = 27a (Fig. 3.12e), D = 35a (Fig. 3.12i), D = 43a (Fig. 3.12m) and D = 51a (Fig. 3.12q). The cavities were optically pumped at room temperature with a pulsed laser (wavelength λ = 1,064 nm, pulse time T = 12 ns at a repetition rate f = 215 kHz) and the emission from each aperture was collected through a confocal microscope optimized for near-infrared spectroscopy (Supplementary Information).
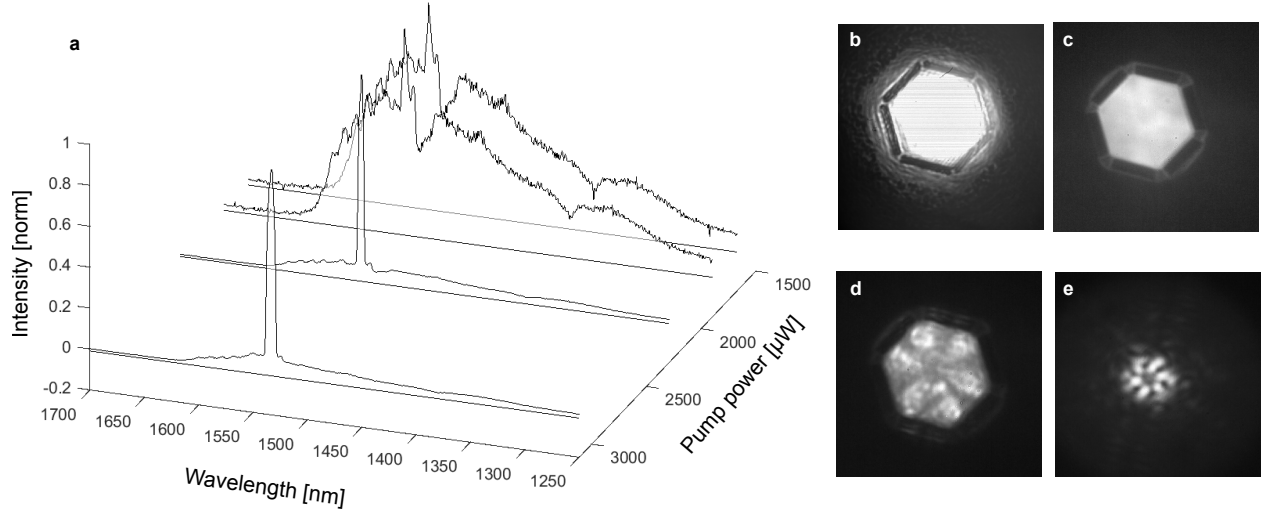
Figure 3.11: *Measured sprectum as a function of the pump power and infrared camera images of the BerkSEL and its far field.* **(a)** The evolution of the normalized emission spectrum of a BerkSEL. As the pump power is increased a clear transition from broad spontaneous emission to a narrow lasing peak is observed. **(b-e)** IR camera image of a BerkSEL **(b)** without any filter, **(c)** with a > 1100 nm long-pass filter under spontaneous emission, **(d)** in the stimulated emission regime, and **(e)** its far field beam profile.

The signal was directed towards a monochromator coupled to a indium-gallium-arsenide photodiode for spectral measurements. Figure 4 presents the evolution of the normalized output power as a function of the wavelength and the size of the cavity for unit-cell hole radii smaller than the singular radius r_{Dirac} (Fig. 3.12b,f,j,n,r), equal to r_{Dirac} (Fig. 3.12c,g,k,o,s) and greater than r_{Dirac} (Fig. 3.12d,h,l,p,t). For D = 19a, cavities are single mode for $r < r_{\text{Dirac}}$ (Fig. 3.12b), $r \sim r_{\text{Dirac}}$ (Fig. 3.12c) and $r > r_{\text{Dirac}}$ (Fig. 3.12d). For D = 27a, cavities remain single mode for $r < r_{\text{Dirac}}$ (Fig. 3.12f), $r \sim r_{\text{Dirac}}$ (Fig. 3.12g) and $r > r_{\text{Dirac}}$ (Fig. 3.12h). This is because these cavities are relatively small. However, when the size of cavities is increased to D = 35a or larger, we observe that they become multimode for $r < r_{\text{Dirac}}$ (Fig. 3.12j,n,r), remain single mode for $r \sim r_{\text{Dirac}}$ (Fig. 3.12k,o,s) and become multimode for $r > r_{\text{Dirac}}$ (Fig. 3.12l,p,t). The Dirac singularity erases higher-order modes in open-Dirac cavities and BerkSELs remain single mode when their size is increased. It is worth noting that the uniform field profile across the aperture for the fundamental mode (Fig. 2.12) and the non-vanishing free spectral range (Fig. 3.6) depletes gain across the aperture, making it more difficult for higher-order modes to lase. Single-mode lasing is thus maintained in BerkSELs even for near-damage-threshold pump power. BerkSELs are thus robust to size and pump power density scaling because of the non-vanishing complex free spectral range and the participation of all unit cells (or resonators) in the aperture to the lasing mode. These experiments validate our theory and make BerkSELs scale-invariant surface-emitting
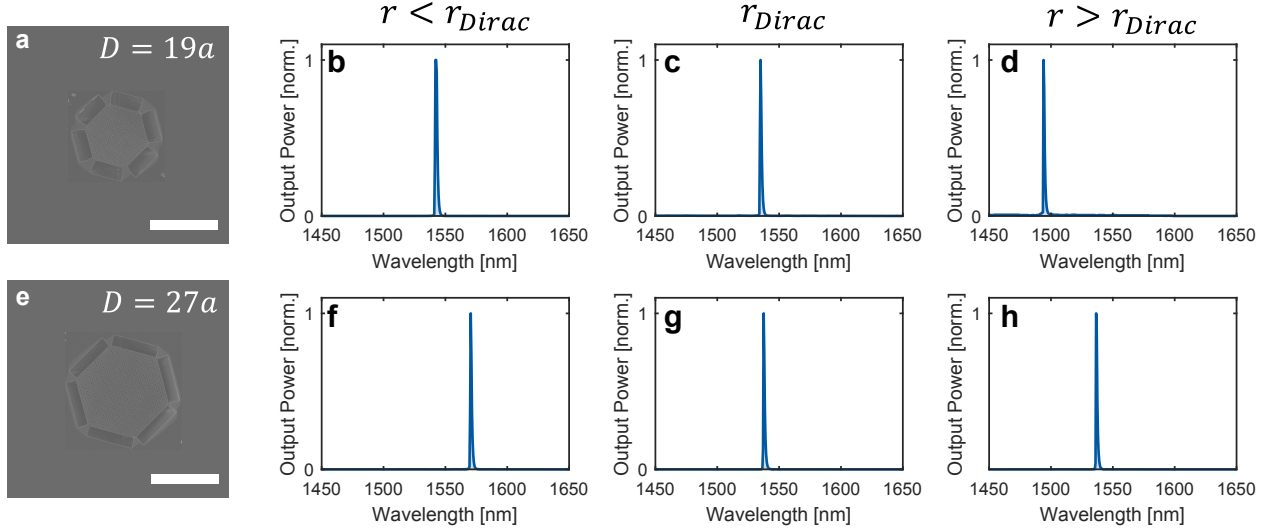
Figure 3.12: *Single-mode emission from small photonic crystal lasers.* **(a,e)** Top-view SEM of fabricated open-Dirac cavities of size **(a)** $D = 19a$, and **(e)** $D = 27a$, where D is the diameter of the aperture and a is the size of the unit cell of the PhC. Scale bars, $25\,\mu\text{m}$. **(b–d,f–h)** Evolution of the normalized output power as a function of the wavelength and the size of the cavity for unit-cell hole radii **(b,f)** smaller than the singular radius r_{Dirac}, **(c,g)** equal to r_{Dirac}, and **(d,h)** greater than r_{Dirac}. The pump power density is $1.1\,\mu\text{W}\mu\text{m}^{-2}$ in all cases. For $D = 19a$, cavities are single mode for **(b)** $r < r_{\text{Dirac}}$, **(c)** $r \sim r_{\text{Dirac}}$, and **(d)** $r > r_{\text{Dirac}}$. For $D = 27a$, cavities are single mode for **(f)** $r < r_{\text{Dirac}}$, **(g)** $r \sim r_{\text{Dirac}}$, and **(h)** $r > r_{\text{Dirac}}$.

lasers. The apparent high threshold power density of our BerkSELs originates from surface recombination as we are directly structuring the quantum wells, and it is comparable to previously reported lasers using a similar strategy [53]. This can be alleviated by designing alternative structures or by additional chemical treatments of the devices. BerkSELs are, in principle, infinitely scalable if the proposed open-Dirac potential can be implemented exactly. In practice, considerations such as proximity effects in lithography, electrical injection or heat release will need to be addressed for high-power devices. Assuming typical fabrication imperfections with a variation of hole radii on the order of 5 nm, the fundamental mode is found to be robust to disorder (Supplementary Information).

To further characterize the single-mode lasing of BerkSELs, we present in Fig. 3.14 the light–light curve (Fig. 3.14a), the second-order autocorrelation at zero-delay $\text{g}^2(\tau = 0)$ (Fig. 3.14b) and its pulse width (Fig. 3.14c). The three different regimes corresponding to spontaneous emission (blue region), amplified spontaneous emission (ASE) (yellow region) and stimulated emission (red region) are observed as the pump power is increased. The second-order autocorrelation function shows a transition from spontaneous emission to ASE
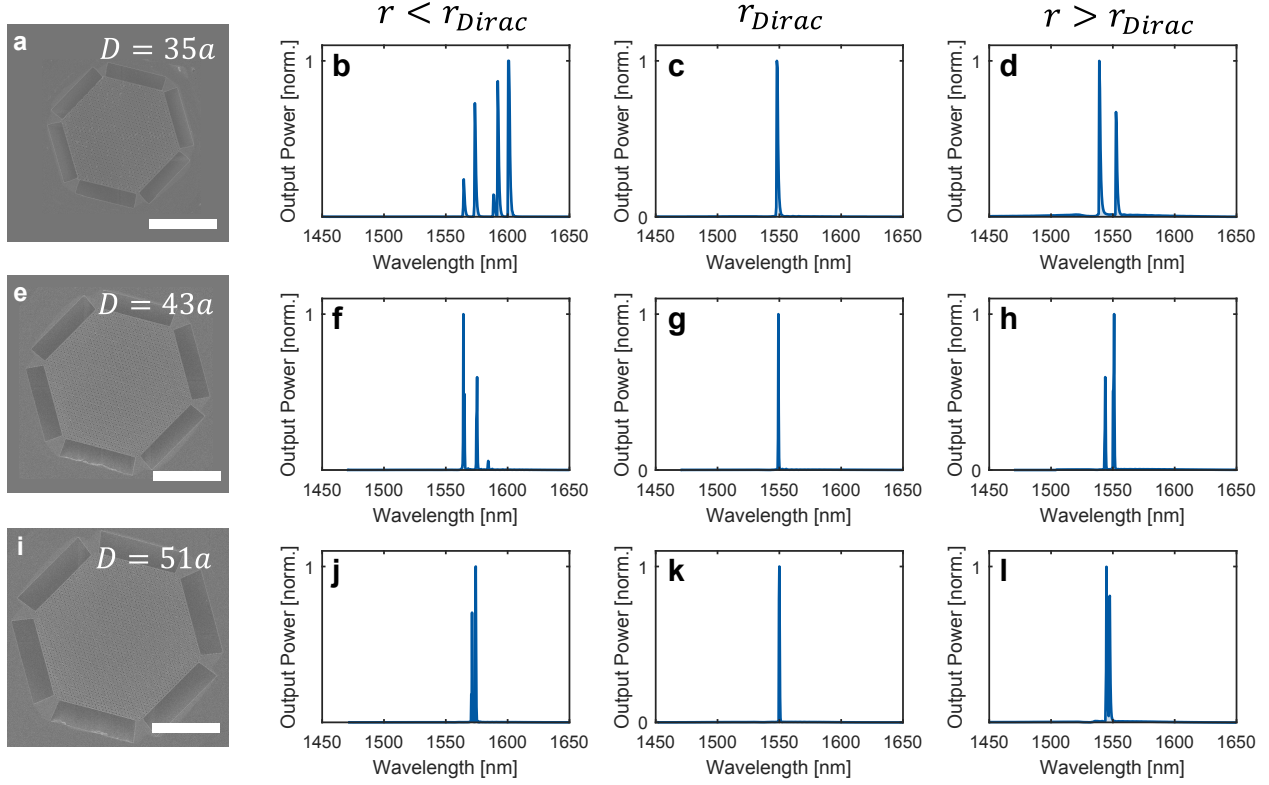
Figure 3.13: *Single-mode selectivity in BerkSELs.* **(a,e,i)** Top-view SEM of fabricated open-Dirac cavities of size **(a)** $D = 35a$, **(e)** $D = 43a$, **(i)** $D = 51a$, where D is the diameter of the aperture and a is the size of the unit cell of the PhC. Scale bars, $25\,\mu$m. **(b–d,f–h,j–l)** Evolution of the normalized output power as a function of the wavelength and the size of the cavity for unit-cell hole radii **(b,f,j)** smaller than the singular radius r_{Dirac}, **(c,g,k)** equal to r_{Dirac}, and **(d,h,l)** greater than r_{Dirac}. The pump power density is $1.1\,\mu$Wμm^{-2} in all cases. When the size is increased to $D = 35a$, $D = 43a$ and $D = 51a$, we observe that cavities become multimode mode for **(b,f,j)** $r < r_{\text{Dirac}}$, remain single mode for **(c,g,k)** $r \sim r_{\text{Dirac}}$, and become multimode again for **(d,h,l)** $r > r_{\text{Dirac}}$.

as its width drops sharply and the bunching $g^2(0)$ increases. The transition from ASE to stimulated emission is evident from $g^2(0)$ decreasing to unity (Fig. 3.14b) and the width gradually increasing after the lasing threshold (Fig. 3.14c), unambiguously proving single-mode lasing action from BerkSELs [54, 55]. To confirm that lasing originates from the theoretically predicted B mode (Figs. 2.12 and 3.6), experimental far fields (Fourier space images) of BerkSELs under optical pumping are presented for cavity sizes of D = 11a (Fig. 3.14d), D = 19a (Fig. 3.14e), D = 27a (Fig. 3.14f), D = 35a (Fig. 3.14g) and D = 51a (Fig. 3.14h).

The six-fold symmetry of the beams match with the far-field obtained from simulations of finite cavities (Fig. 3.5) which originate from the B mode with a topological charge of two.
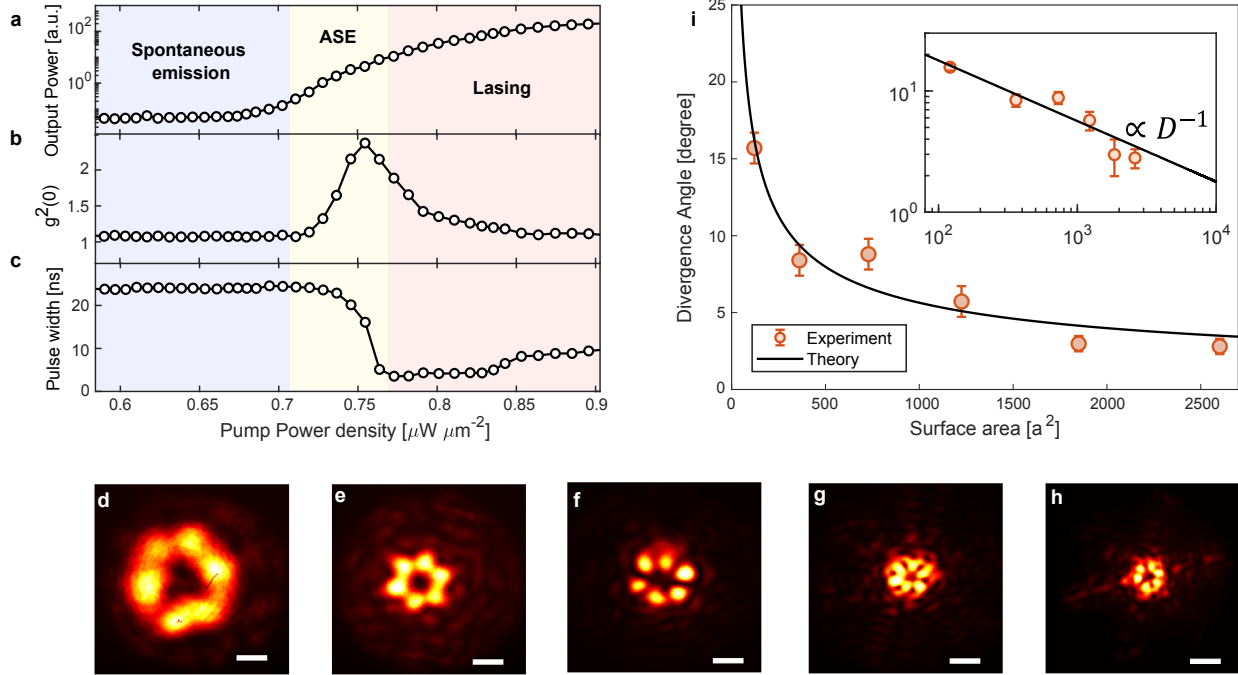
Figure 3.14: *Photon statistics and far field of the BerkSEL.* **(a)** Emitted output power of a BerkSEL of aperture diameter D = 35a (where a is the size of the unit cell) as a function of the average pump power density (light–light curve). **(b,c)** Second-order intensity auto-correlation measurements **(b)** at zero-delay $g^2(0)$, and **(c)** its pulse width. The pulse width of the second-order autocorrelation function shows a distinct transition from spontaneous emission to ASE as the width drops sharply and then from ASE to stimulated emission as the width gradually increases. These transitions unambiguously demonstrate single-mode lasing from BerkSELs. Experimental far fields (Fourier space images) of BerkSELs under optical pumping are presented for cavity sizes of **(d)** D = 11a, **(e)** D = 19a, **(f)** D = 27a, **(g)** D = 35a, and **(h)** D = 51a. Scale bars, 10°. **(i)** Measured and theoretical beam divergence angle as a function of the cavity size. The continuous line is the theoretical prediction and markers are experimental data. A good agreement is observed between theory and experiments. The inset shows the same data plotted on a log–log scale, demonstrating the 1/D scaling of the beam divergence where D is the diameter of the aperture (Supplementary Information). This scaling corresponds to the theoretical limit obtained for modes with a flat envelope fully covering an aperture. Error bars indicate the standard deviation of the beam divergence.

Scaling up the cavity size manifests in a smaller beam divergence as expected. We plotted the measured beam divergence as a function of the size of the cavity in Fig. 3.12i. The measured beam divergence matches with our theory and scales as $1/D$, in full agreement with theory for modes with a flat envelope fully covering an aperture.[1]

In this chapter, we have successfully demonstrated the concept of scale-invariant surface-emitting lasers using open-Dirac cavities. These cavities effectively suppress higher-order modes by merging the fundamental band with more lossy bands, a pivotal attribute of our design. The fundamental mode's flat envelope ensures uniform participation of all resonators within the aperture, contributing to the single-mode lasing. Our experimental verification, including second-order intensity correlation measurements and far-field emission studies, aligns with theoretical expectations. These findings underscore the critical role of boundaries and mode admixtures in reciprocal space, setting a new precedent for scaling in various wave-based. The practical simplicity and universal applicability of BerkSELs make them an ideal choice for diverse applications, ranging from virtual reality and lidar to data centers, defense, and medical imaging technologies.

---

[1]The Regents of the University of California have filed a patent on systems, methods and applications using the principles described in this thesis.

Chapter 4

Conclusion

We now stand at the intersection of theoretical exploration and practical application. It is evident that understanding the theory and analyzing just one possible implementation of the Berkeley surface-emitting laser (BerkSEL) is only the initial step in a much larger journey. To transform a promising technological concept into an actual device, we must map a path for the future and address its current limitations. For the BerkSEL, this evolution is pivotal in transcending laboratory success to potentially become the next generation of semiconductor lasers.

4.1 Technological Roadmap

A critical milestone practical applicability is the transition from optical to electrical pumping. Electrical operation directly impacts a laser's efficiency, power output, and footprint—key metrics that define the usability and adaptability of laser technology in real-world scenarios. Hence, this transition is not merely a technical improvement; it represents a significant advancement in how the technology can be deployed and integrated into a myriad of applications, ranging from high-speed communication networks to precision sensing in complex environments.

One possible albeit simple scheme to achieve electrical operation is presented in Fig. 4.1a. The semiconductor stack consists of a p-i-n junction to coax recombination of electrons and holes in the undoped region where the bulk of the photonic mode is localized. However, overlap of the electromagnetic field with the doped regions introduces material losses due to free-carrier absorption. These losses scale linearly with the dopant concentration and hence the smalles possible doping is desirable from the photonics perspective. Unfortunately, free carriers are necessary to achieve electrical conduction. As shown in Fig. 4.1b, the current rapidly saturates as the doping concentration drops. It is thus crucial to reach a compromise between conductivity and optical losses in order to design an efficient electrically operated semiconductor laser.

The presence of a BIC mode near the band edge can partially resolve this issue. In
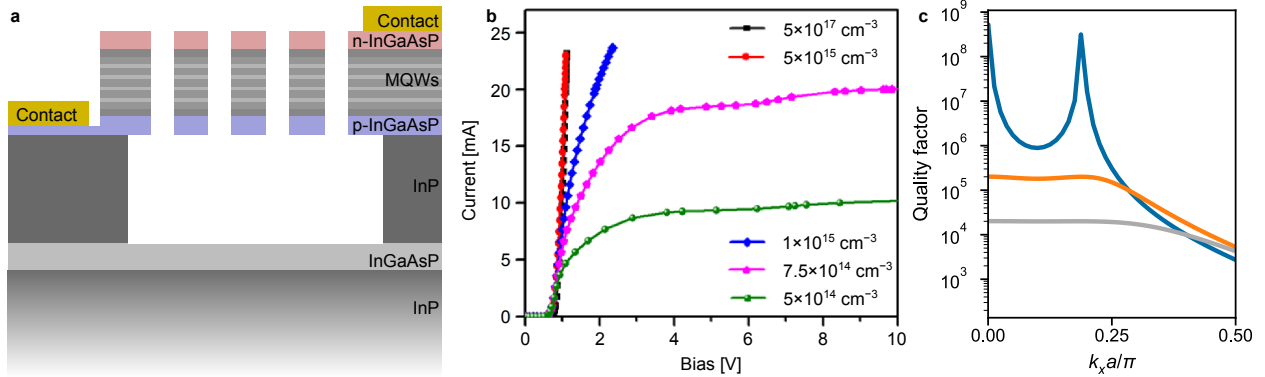
Figure 4.1: *Electrical pumping scheme and influence of doping on lateral carrier injection.* **(a)** A simple schematic for lateral current injection in a suspended photonic crystal. Electrons travel from the top electrode on the right through the n-doped semiconductor and should ideally recombine with the holes in the center of the suspended region. **(b)** Reducing the doping concentration in the doped layers results in a nonlinear IV curve and rapid saturation of the current at low doping levels. **(c)** Influnce of doping concentration on the quality factor dispersion in momentum space. Increasing dopant level reduce the peak Q but off-Γ BICs can mitigate this effect. The free-carrier induced losses create a plateau of strong photon confinement across a wide momentum range which is desirable for low-threshold lasing in small cavities.

Fig. 4.1c, the quality factor of band with a symmetry-protected and non-symmetry-protected BIC is plotted for three different doping concentrations. Indeed, the quality factor of the electromagnetic mode drops as the concentration of impurities increases. Intrestingly we also notice that due to the presence of the off-Γ BIC, a broad plateau of the quality factor is observed in momentum space. This is favorable for small devices as the δ_k is large and the loss rates are typically high even in undoped cavities. Thus, low-threshold lasing can be achieved in such structures provided the cavity size is small. As the cavity size increases however, the recombination no longer occurs near the center of the devices. Free (conduction band) electrons from the n-doped layer move a lot faster than the holes (or valence band electrons) and light emission only occurs near the p-contact. Various approaches have been investigated to mitigate this including the use of narrow posts or dielectric mirrors and will be necessary to be integrated into the BerkSEL as a key next step in its development.

4.1.1 Capabilities and applications

The BerkSEL, in its current form, already exhibits other remarkable qualities such as vortex beam emission and propensity for high-power emission. Furthermore, envelope control in open-Dirac cavities allows for dynamic beam steering capabilities, making it an attractive

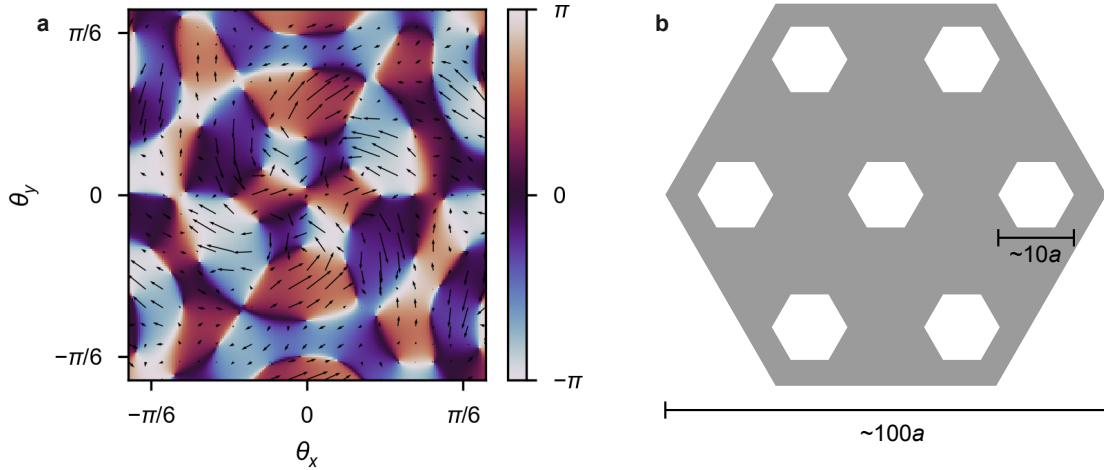option for advanced optical systems such as LIDAR and high-resolution imaging.

Figure 4.2: *Vortex emission and strategy for high-power emission in BerkSELs.* **(a)** The polarization vortex of BerkSELs predicted by electromagnetic simulations. **(b)** Potential design modification to increase the power output of BerkSELs while maintaining single mode operation. Defects which maintain six fold symmetry could be introduced into a large cavity to increase radiative losses and control beam characteristics.

Optical trapping

Conventionally, the force gradient in a sharply focused beam of light is used to trap charged particles within the desired region in space. Careful manipulation of the beam can also be used as optical tweezers to move the particle around. The winding in the polarization of a beam can further improve these characteristics of light. The vortex nature of the electric field creates a deep potential well in the center trapping particles like neutral atoms, charged ions, as well as microbiological specimen. Polarization vortex can also be converted into a phase vortex which imparts orbital angular momentum to the electromagnetic field. This momentum can be transferred to the trapped particle that would then start spinning allowing for the study of angular dynamics in fundamental particles. The far field polarization emitted by BerkSELs illustrated in Fig. 4.2a is ideal for such manipulation.

Dynamic beam steering

The emission angle of the fundamental lasing mode is determined by the location of the mode in momentum space. The in-plane Bloch momentum is related to the emission angle

θ by,

$$|\boldsymbol{k}_{\parallel}| = |\boldsymbol{k}| \sin\theta \,. \tag{4.1}$$

In Fig. 2.11 we discovered how the momentum of the fundamental mode can be controlled all the way from zero to π/D, where D is the linear dimension of the cavity. This envelope wavevector is a direct consequence of the boundary conditions around the edges of the cavity. Hence, if we change the surrounding environment by controlling the permittivity of the material around the cavity we can introduce a shift in the in-plane momentum and as a result, the emission angle of the beam. This property can find valuable utility in small-scale, low-power LIDARs deployed on drons and micro-robots.

High-power lasers

The scale-invariant nature of the flat envelope fundamental mode is particularly attractive for applications that require high power density such as industrial manufacturing, long range detection, defense, and even for far-fetched ideas such as light-sail propulsion of satellites. In its current form, BerkSEL is optimized for a simple geometry and direct observation for the underlying physics. This means that the quality factor of the B_1 and E_2 Bloch modes is very high and they do not easily radiate. This works well for a laboratory environment where achieving a lasing operation is sufficient. However, for a truly high power output, the cavity or the unit cell should be modified to introduce radiation channels for the power within the cavity to be coupled out. One possible way to do this is by placing the open-Dirac cavity on a substrate which also helps with dissipating the heat generated in a device emitting a large amount of energy. Further strategies could include designing leakage channels by patterning the cavity at the scale of a few 10s of unit cells as illustrated in Fig. 4.2b. This has the added advantage of enabling control over the far field of the emitted beam.

   Beyond lasers, the principles underlying the open-Dirac cavity design have broader implications. The unique dispersion properties offer exciting possibilities in nonlinear optics, potentially enhancing the efficiency of frequency conversion processes. In the realm of quantum communications, the BerkSEL's design could contribute to the development of more secure and efficient communication systems. Furthermore, its application in fundamental research could lead to new discoveries, particularly in the study of light-matter interactions and cavity quantum electrodynamics.

4.2   Ending notes

The exploration of wave dynamics in various physical systems, from photonics and acoustics to quantum mechanics, has been a cornerstone of advancing modern technologies. In particular, the controlling wave behavior through manipulating potential distributions plays a pivotal role in these disciplines. The concept of Dirac cones, initially prominent in the study of electronic properties of materials like graphene, has transcended its origins to become a fundamental aspect in the understanding of wave dynamics in diverse systems. Over the

course of this investigation, we have extended this concept to the realm of open-Dirac potentials, where the interplay between linear dispersion and open boundary conditions can be engineered to design a scalable single-mode laser cavity. We have further eshtablished a generalized theoretical framework for open-Dirac cavities that is applicable across wave-based physical systems regardless of the specific implementation. We explored how these potentials can be employed in photonic crystal slab cavities to create unconventional intensity distributions. The ability to produce modes with a flat envelope and control the wavevector of the cavity mode marks a significant improvement in the control over light-matter interaction in cavities. By experimentally validating the predicted cavity states in photonic crystal slabs, our research not only corroborates theoretical predictions but also demonstrates practical control over field distribution at both the unit cell and cavity scales. The implications of this study extend beyond photonics, offering insights into wave dynamics that could revolutionize a range of technological applications.

As this dissertation reaches its conclusion, it is pertinent to reflect on the journey undertaken and the significant milestones achieved. Throughout this work, we have delved into the intricate world of semiconductor lasers, with a particular focus on the development and characterization of the Berkeley surface-emitting laser (BerkSEL). We embarked on this journey acknowledging the challenges inherent in scaling up laser cavities while preserving single-mode operation, a critical aspect for a myriad of applications ranging from data transmission to material processing.

The journey from theoretical exploration to tangible innovation exemplified in the BerkSEL is a testament to the transformative power of interdisciplinary research. Bridging concepts from condensed matter physics, quantum mechanics, and electrical engineering, I hope that this work has not only contributed to the academic discourse but has also paved the way for practical advancements in photonics.

Bibliography

1. Schawlow, A. L. & Townes, C. H. Infrared and Optical Masers. *Physical Review* **112,** 1940–1949 (1958).

2. Contractor, R. *et al.* Scalable single-mode surface-emitting laser via open-Dirac singularities. *Nature* (2022).

3. Siegman, A. E. *Lasers* 1322 pp. (University Science Books, 1986).

4. Einstein, A. Zur Quantentheorie der Strahlung. *Physikalische Zeitschrift* **18,** 121–128 (1917).

5. Schrödinger, E. An Undulatory Theory of the Mechanics of Atoms and Molecules. *Physical Review* **28,** 1049–1070 (1926).

6. Maxwell, J. C. VIII. A dynamical theory of the electromagnetic field. *Philosophical Transactions of the Royal Society of London* **155,** 459–512 (1997).

7. Bloch, F. Über die Quantenmechanik der Elektronen in Kristallgittern. *Zeitschrift für Physik* **52,** 555–600 (1929).

8. Sakoda, K. *Optical properties of photonic crystals* 2nd ed. *Springer series in optical sciences* **80.** 253 pp. (Springer, Berlin ; New York, 2005).

9. Baym, G. *Lectures on Quantum Mechanics* 1–594 (CRC Press, 1969).

10. Von Neumann, J. & Wigner, E. P. in *The Collected Works of Eugene Paul Wigner* 291–293 (Springer Berlin Heidelberg, Berlin, Heidelberg, 1993).

11. Stillinger, F. H. & Herrick, D. R. Bound states in the continuum. *Physical Review A* **11,** 446–454 (1975).

12. Friedrich, H. & Wintgen, D. Interfering resonances and bound states in the continuum. *Physical Review A* **32,** 3231–3242 (1985).

13. Griffiths, D. J. & Schroeter, D. F. *Introduction to Quantum Mechanics* (Cambridge University Press, 2018).

14. Stillinger, F. Potentials supporting positive-energy eigenstates and their application to semiconductor heterostructures. *Physica B+C* **85,** 270–276 (1976).

15. Friedrich, H. & Wintgen, D. Physical realization of bound states in the continuum. *Physical Review A* **31,** 3964–3966 (1985).

16. Silveirinha, M. G. Trapping light in open plasmonic nanostructures. *Physical Review A* **89,** 023813 (2014).

17. Marinica, D. C., Borisov, A. G. & Shabanov, S. V. Bound States in the Continuum in Photonics. *Physical Review Letters* **100,** 183902 (2008).

18. Bulgakov, E. N. & Sadreev, A. F. Bound states in the continuum in photonic waveguides inspired by defects. *Physical Review B* **78,** 075105 (2008).

19. Ndangali, R. F. & Shabanov, S. V. Electromagnetic bound states in the radiation continuum for periodic double arrays of subwavelength dielectric cylinders. *Journal of Mathematical Physics* **51,** 102901 (2010).

20. Hsu, C. W. *et al.* Observation of trapped light within the radiation continuum. *Nature* **499,** 188–191 (2013).

21. Moharam, M. G. & Gaylord, T. K. Rigorous coupled-wave analysis of planar-grating diffraction. *Journal of the Optical Society of America* **71,** 811 (1981).

22. Ko, D. Y. K. & Sambles, J. R. Scattering matrix method for propagation of radiation in stratified media: attenuated total reflection studies of liquid crystals. *Journal of the Optical Society of America A* **5,** 1863–1866 (1988).

23. Azzam, S. I., Shalaev, V. M., Boltasseva, A. & Kildishev, A. V. Formation of Bound States in the Continuum in Hybrid Plasmonic-Photonic Systems. *Physical Review Letters* **121,** 253901 (2018).

24. Gao, X. *et al.* Formation mechanism of guided resonances and bound states in the continuum in photonic crystal slabs. *Scientific Reports* **6,** 31908 (2016).

25. Reed, M. & Simon, B. *Methods of Modern Mathematical Physics. III: Scattering Theory* 1st, 1–463 (Academic Press, 1979).

26. Ndao, A. *et al.* Differentiating and quantifying exosome secretion from a single cell using quasi-bound states in the continuum. *Nanophotonics* **9,** 1081–1086 (2020).

27. Zhen, B., Hsu, C. W., Lu, L., Stone, A. D. & Soljačić, M. Topological Nature of Optical Bound States in the Continuum. *Physical Review Letters* **113,** 257401 (2014).

28. Lepetit, T. & Kanté, B. Controlling multipolar radiation with symmetries for electromagnetic bound states in the continuum. *Physical Review B* **90,** 241103 (2014).

29. Chen, W., Chen, Y. & Liu, W. Singularities and Poincar\'{e} Indexes of Electromagnetic Multipoles, 1–10. arXiv: `1901.04159` (2019).

30. Novoselov, K. Electric field effect in atomically thin carbon films. en. *Science* **306,** 666–669 (2004).

31. Haldane, F. Model for a quantum Hall effect without Landau levels: condensed-matter realization of the "parity anomaly". en. *Phys. Rev. Lett* **61,** 2015–2018 (1988).

32. Sakoda, K. Universality of mode symmetries in creating photonic Dirac cones. en. *J. Opt. Soc. Am. B* **29,** 2770 (2012).

33. Sakoda, K. Proof of the universality of mode symmetries in creating photonic Dirac cones. en. *Opt. Express* **20,** 25181 (2012).

34. Enoch, S., Tayeb, G., Sabouroux, P., Guérin, N. & Vincent, P. A metamaterial for directive emission. en. *Phys. Rev. Lett* **89,** 213902 (2002).

35. Huang, X., Lai, Y., Hang, Z., Zheng, H. & Chan, C. Dirac cones induced by accidental degeneracy in photonic crystals and zero-refractive-index materials. es. *Nat. Mater* **10,** 582–586 (2011).

36. Moitra, P. Realization of an all-dielectric zero-index optical metamaterial. en. *Nat. Photon* **7,** 791–795 (2013).

37. Li, Y. On-chip zero-index metamaterials. en. *Nat. Photon* **9,** 738–742 (2015).

38. Liberal, I. & Engheta, N. Near-zero refractive index photonics. es. *Nat. Photon* **11,** 149–158 (2017).

39. Jacqmin, T. Direct observation of Dirac cones and a flatband in a honeycomb lattice for polaritons. en. *Phys. Rev. Lett* **112,** 116402 (2014).

40. Lowe, J. P. & Peterson, K. A. *Quantum Chemistry* 736 pp. (Elsevier Academic Press, 2006).

41. Gelessus, A., Thiel, W. & Weber, W. Multipoles and Symmetry. *Journal of Chemical Education* **72,** 505 (1995).

42. Kogelnik, H. & Shank, C. Stimulated emission in a periodic structure. en. *Appl. Phys. Lett* **18,** 152–154 (1971).

43. Soda, H., Iga, K., Kitahara, C. & Suematsu, Y. GaInAsP/InP surface emitting injection lasers. en. *Jpn J. Appl. Phys* **18,** 2329–2330 (1979).

44. Meier, M. Laser action from two-dimensional distributed feedback in photonic crystals. en. *Appl. Phys. Lett* **74,** 7–9 (1999).

45. Imada, M. Coherent two-dimensional lasing action in surface-emitting laser with triangular-lattice photonic crystal structure. en. *Appl. Phys. Lett* **75,** 316–318 (1999).

46. Choquette, K., Hou, H., Geib, K. & Hammons, B. *Uniform and high power selectively oxidized 8x8 VCSEL array* en. in *IEEE/LEOS Summer Topical Meetings 11–12 (IEEE* (1997).

47. Francis, D., Chen, H.-L., Yuen, W., Li, G. & Chang-Hasnain, C. Monolithic 2D-VCSEL array with 2 W CW and 5 W pulsed output power. en. *Electron. Lett* **34,** 2132–2133 (1998).

48. Yoshida, M. Double-lattice photonic-crystal resonators enabling high-brightness semiconductor lasers with symmetric narrow-divergence beams. en. *Nat. Mater* **18,** 121–128 (2019).

49. Bravo-Abad, J., Joannopoulos, J. & Soljacic, M. Enabling single-mode behavior over large areas with photonic Dirac cones. en. *Proc. Natl Acad. Sci. USA* **109,** 9761–9765 (2012).

50. Chua, S.-L., Lu, L., Bravo-Abad, J., Joannopoulos, J. & Soljačić, M. Larger-area single-mode photonic crystal surface-emitting lasers enabled by an accidental Dirac point. it. *Opt. Lett* **39,** 2072–2075 (2014).

51. Gao, X. Dirac-vortex topological cavities. pt. *Nat. Nanotechnol* **15,** 1012–1018 (2020).

52. Siegman, A. *Lasers 466–472 (Univ* en (Science Book, 1986).

53. Kodigala, A. *et al.* Lasing action from photonic bound states in continuum. *Nature* **541,** 196–199 (2017).

54. Loudon, R. *The Quantum Theory of Light* 3rd edn. en (Oxford Univ. Press, 2000).

55. Pan, S., Gu, Q., El Amili, A., Vallini, F. & Fainman, Y. Dynamic hysteresis in a coherent high- nanolaser. es. *Optica* **3,** 1260–1265 (2016).